



# 1 Global Evaluation of the Ecosystem Demography Model (ED

## 2 v3.0)

3

4 Lei Ma<sup>1</sup>, George Hurtt<sup>1</sup>, Lesley Ott<sup>2</sup>, Ritvik Sahajpal<sup>1</sup>, Justin Fisk<sup>3</sup>, Rachel Lamb<sup>1</sup>, Hao Tang<sup>1,7</sup>,

5 Steve Flanagan<sup>4</sup>, Louise Chini<sup>1</sup>, Abhishek Chatterjee<sup>2,5</sup>, Joseph Sullivan<sup>6</sup>

6 <sup>1</sup> Department of Geographical Sciences, University of Maryland, College Park, MD 20770, USA

7 <sup>2</sup> Global Modeling and Assimilation Office, NASA Goddard Space Flight Center, Greenbelt, MD 20771, USA

8 <sup>3</sup> Regrow Agriculture Inc., Durham, NH 03824, USA

9 <sup>4</sup> Wildland Fire Science, Tall Timbers Research Station and Land Conservancy, Tallahassee, FL 32312, USA

10 <sup>5</sup> Universities Space Research Association, Columbia, MD 21046, USA

11 <sup>6</sup> Department of Plant Science & Landscape Architecture, University of Maryland, College Park, MD 20770, USA

12 <sup>7</sup> Department of Geography, National University of Singapore, 117570, Singapore

13

14 *Correspondence to:* Lei Ma (lma6@umd.edu)

15

### 16 **Abstract.**

17 Terrestrial ecosystems play a critical role in the global carbon cycle but have highly uncertain future dynamics.

18 Ecosystem modelling that includes the scaling-up of underlying mechanistic ecological processes has the potential

19 to improve the accuracy of future projections, while retaining key process-level detail. Over the past two decades,

20 multiple modelling advances have been made to meet this challenge, including the Ecosystem Demography (ED)

21 model and its derivatives including ED2 and FATES. Here, we present the global evaluation of the Ecosystem

22 Demography model (ED v3.0), which like its predecessors features the formal scaling of physiological processes of

23 individual-based vegetation dynamics to ecosystem scales, together with integrated submodules of soil

24 biogeochemistry and soil hydrology, while retaining explicit tracking of vegetation 3-D structure. This new version

25 builds on previous versions and provides the first global calibration and evaluation, global tracking of the effects of

26 climate and land-use change on vegetation 3-D structure, new spin-up process and input datasets, as well as

27 numerous other advances. Model evaluation was performed with respect to a set of important benchmarking

28 datasets, and model estimates were within observational constraints for multiple key variables including: (i) global

29 patterns of dominant plant functional types (broadleaf vs evergreen); (ii) spatial distribution, seasonal cycle, and

30 interannual trends of global Gross Primary Production (GPP); (iii) global interannual variability of Net Biome

31 Production (NBP); and (iv) global patterns of vertical structure including leaf area and canopy height. With this

32 global model version, it is now possible to simulate vegetation dynamics from local to global scales and from



33 seconds to centuries, with a consistent mechanistic modelling framework amendable to data from multiple  
34 traditional and new remote sensing sources, including lidar.

## 35 **1 Introduction**

36 Terrestrial ecosystems and the associated carbon cycle are of critical importance in providing ecosystem services  
37 and regulating global climate. Plants store approximately 450-650 Pg C as biomass globally. They remove  
38 approximately 120 Pg C from the atmosphere each year through photosynthesis, and release a similar magnitude of  
39 carbon to the atmosphere through respiration (Beer et al., 2010; Ciais et al., 2014a). Human activities over past  
40 centuries have significantly impacted terrestrial ecosystems through biophysical and biogeochemical mechanisms  
41 (Cramer et al., 2001; Walther et al., 2002; Brovkin et al., 2004; Pielke Sr. et al., 2011). Quantification, attribution  
42 and future projections of the terrestrial carbon sink requires in-depth understanding of underlying ecological  
43 processes and their sophisticated responses and feedbacks to climate change, elevated CO<sub>2</sub>, and land use and land  
44 cover change (LULCC) across multiple biomes and spatial and temporal scales (Canadell et al., 2007; Erb et al.,  
45 2013; Keenan and Williams, 2018). This demand for information has driven the emergence and development of  
46 dynamic global ecosystem models (DGVMs), which simplify the structure and functioning of global vegetation into  
47 several plant functional types and simulate vegetation distribution and associated biogeochemical and hydrological  
48 cycles with ecophysiological principles (Prentice et al., 2007; Prentice and Cowling, 2013). The first generation of  
49 DGVMs have been used successfully to address a variety of carbon cycle related questions and integrated into Earth  
50 System Models (ESMs) (Cramer et al., 2001; Sitch et al., 2008). Subsequent developments have improved the  
51 representation of vegetation demographic processes within ESMs, including the Ecosystem Demography model  
52 (ED) (Hurtt et al., 1998; Moorcroft et al., 2001), ED2 (Medvigy 2006; Medvigy et al., 2009; Longo et al., 2019a),  
53 CLM(ED) (Fisher et al., 2015; Lawrence et al., 2019; Massoud et al., 2019), SEIB-DFVM (Spatially-Explicit  
54 Individual-based Dynamic Global Vegetation Model) (Sato et al., 2007), LPJ-GUESS (Lund-Postdam-Jena General  
55 Ecosystem Simulator) (Smith et al., 2001, 2014) and GFDL-LM3-PPA (Geophysical Fluid Dynamics Laboratory  
56 Land Model 3 with the Perfect Plasticity Approximation) (Weng et al., 2015), as summarized in Fisher et al., 2018.

57  
58 In addition to model development, model evaluation is an important process to assess model uncertainties and also  
59 identify processes that need particular improvements (Anav et al., 2013; Luo et al., 2012; Eyring et al., 2019).  
60 Considerable effort has been spent on standardizing evaluation practices and developing a comprehensive  
61 benchmarking system (Abramowitz et al., 2012; Collier et al., 2018; Eyring et al., 2016; Kelly et al., 2013;  
62 Randerson et al., 2009). For example, a benchmarking system from the International Land Model Benchmarking  
63 (ILAMB) project has been increasingly used to evaluate ecosystem and climate models (Collier et al., 2018;  
64 Ghimire et al., 2016; Luo et al., 2012). In parallel, new observations are providing new opportunities to initialize and  
65 test models. Of particular relevance for ecosystem models is the advent of spaceborne lidar missions (i.e., GEDI and  
66 ICESat-2) (Dubayah et al., 2020a; Markus et al., 2017), which provide unprecedented global observations of forest  
67 structure, including vertical distribution of leaf foliage. Building on this past work, and utilizing new observations,  
68 an updated and systematic evaluation of model performance on multiple variables is now possible.



69

70 Here, we present the global evaluation of Ecosystem Demography v3.0. The ED model was developed two decades  
71 ago using a formal scaling approach (Size- and Age-Structured approximation, SAS) to efficiently approximate the  
72 expected dynamics of individual based forest dynamics (Hurtt et al., 1998; Moorcroft et al., 2001). Since its  
73 emergence, the ED model has been continuously developed and applied at various regions and spatial scales, with  
74 land-use changes, and lidar observations (Hurtt et al., 2002, 2004). In the original paper, the model was implemented  
75 at site scale and primarily evaluated for aboveground biomass accumulation during succession using  
76 chronosequence field data, and at the regional scale using 1-degree resolution data on potential biomass, soil carbon  
77 and net primary productivity (NPP) (Moorcroft et al., 2001). Most recently, ED was implemented at high spatial  
78 resolution (90 m) over a regional domain of the Northeastern United States and evaluated for aboveground biomass  
79 using wall-to-wall lidar-based estimates of contemporary biomass at that spatial resolution (Hurtt et al., 2019a; Ma  
80 et al., 2021). The evaluation included >30 million grid cell pairs, and >10<sup>3</sup> forest inventory plots. This progression  
81 spans a range of model capabilities, spatial resolutions, and evaluation data ranging from coarse resolution potential  
82 vegetation, to high spatial resolution contemporary conditions at regional scales. However, development and  
83 evaluation of ED at global scale for contemporary conditions has not yet been accomplished. In this study, ED v3.0  
84 is evaluated at global scales for the first time. Multiple key variables are considered in the evaluation, including  
85 benchmark datasets on vegetation distribution, vegetation structure, and carbon and water fluxes.

## 86 **2 Methods**

87 ED v3.0 is built upon a series of previous model developments (Moorcroft et al., 2001; Hurtt et al., 2002; Albani et  
88 al., 2006; Fisk, 2015; Flanagan et al., 2019). To extend ED's capabilities globally, several additional modifications  
89 were introduced to capture global vegetation distribution across biomes and related carbon stocks and fluxes. Below,  
90 a summary of the ED approach and recent modifications is provided. The full descriptions of each submodule can be  
91 found in the Supplement along with tables of parameter values. To conduct the model evaluation, a model  
92 experimental protocol including equilibrium and transient simulations was developed and relevant forcing data were  
93 identified from global existing datasets. Model simulations were then compared to benchmarking datasets.

### 94 **2.1 Model**

95 The ED model is an individual based prognostic ecosystem model (Moorcroft et al., 2001). By integrating  
96 submodules of growth, mortality, hydrology, carbon cycle, and soil biogeochemistry, ED can track plant dynamics  
97 including growth, mortality, and reproduction. Along with plant dynamics, ED can track the carbon cycle, including  
98 carbon uptake by leaf photosynthesis, carbon allocation to biomass growth in leaves, roots and stems, carbon  
99 redistribution from plants to soil based on plant tissue turnover from dead plants due to mortality and disturbance,  
100 carbon decomposition in various pools (metabolic litter pool, structural litter pool, soil slow pool, soil passive pool,  
101 wood product pool, harvested crop pool, etc) as well as carbon combustion from fire (Fig. 1 and Fig. 2). Over the  
102 last two decades, ED has been continuously developed and combined with lidar and land-use change data to predict



103 ecosystem dynamics and associated water and carbon fluxes across spatial scales (e.g., site to regional and  
104 continental) and temporal scales (e.g., short-term seasonal to long-term decadal and century) (Hurtt et al., 2002,  
105 2004, 2010, 2016, Fisk et al., 2013, Flanagan et al., 2019). ED distinguishes itself from most other ecosystem  
106 models by explicitly tracking vegetation structure and scaling fine-scale physiological processes to large scale  
107 ecosystem dynamics (Hurtt et al., 1998, Moorcroft et al., 2001, Fisher et al., 2018). In ED, vegetation structure (e.g.,  
108 height and diameter at breast height), and physiological processes (e.g., leaf photosynthesis and phenology) are  
109 modelled at the individual scale, where individual plants compete mechanically for light, water, and nutrients.  
110 During implementation, this horizontal heterogeneity is tracked through cohort and patch demography. Explicitly  
111 modelling vegetation height facilitates a potential connection to lidar data. The most advanced version of ED was  
112 used in this study and it has been recently calibrated and evaluated globally by various benchmarking datasets such  
113 as gross primary productivity (GPP), leaf area index (LAI), aboveground biomass (AGB), and net biome  
114 productivity (NBP) (Ma et al., 2021).

### 115 **2.1.1 Additional modifications**

116 Major modifications in ED v3.0 focus on four areas: plant functional type representation, leaf level physiology,  
117 hydrology, and wood products. These areas have been found to be particularly important to improve model  
118 performance globally.

119  
120 Plant functional types describe the characteristics of vegetation in different representative groups for modelling. In  
121 previous ED versions, various PFT combinations were implemented to represent vegetation in the respective regions  
122 where the model was implemented. In the original implementation of ED for Central and South America, four PFTs  
123 were represented (i.e., Early-successional broadleaf, Middle-successional broadleaf, Late-successional broadleaf and  
124 C4 grasses (Moorcroft et al., 2001). In a subsequent implementation over North America, two additional PFTs (i.e.,  
125 Northern pines and Southern pines) were proposed in Albani et al., 2006. Here, these PFTs are included and further  
126 refined as seven major PFTs, namely early-successional broadleaf trees (EaSBT), middle-successional broadleaf  
127 trees (MiSBT), late-successional broadleaf trees (LaSBT), northern and southern pines (NSP), late-successional  
128 conifers (LaSC), C3 shrubs and grasses (C3ShG), and C4 shrubs and grasses (C4ShG) (Supplement S1). The  
129 broadleaf PFTs (i.e., EaSBT, MiSBT, and LaSBT) are distinguished between tropical and non-tropical subtypes.  
130 These PFTs primarily differ in their phenology, leaf physiological traits, allometry, mortality rate, and dispersal  
131 distance. As in previous versions of ED, the spatial distribution of PFTs is mechanistically determined by individual  
132 competition for light, water and nutrients. No quasi-equilibrium climate–vegetation relationships, or other  
133 assumptions or observations, are used to constrain the presence or absence of PFTs.

134

135 Leaf physiology determines short-term (i.e., < hourly) leaf-level carbon and water exchanges in response to  
136 environmental conditions (air temperature, shortwave radiation, air humidity, wind speed, CO<sub>2</sub> level). The  
137 representation of leaf level physiology in previous versions of ED (Moorcroft et al., 2001) was taken from IBIS  
138 (Foley et al., 1998), which in turn was based on prior work from Farquhar, Collatz, Ball and Berry and others



139 (Farquhar and Sharkey 1982; Ball et al., 1987; Collatz et al., 1991, 1992). Here, ED's representation of leaf level  
140 physiology is reformulated for C3 and C4 pathways (Farquhar et al., 1980; Von Caemmerer and Furbank, 1999)  
141 with added boundary layer conductance for diffusing water vapor and CO<sub>2</sub> between ambient air and leaf surface, and  
142 parameterized with temperature dependence functions from other studies (Bernacchi et al., 2001; von Caemmerer et  
143 al., 2009; Kattge and Knorr, 2007; Massad et al., 2007; Von Caemmerer, 2000, Supplement S3).

144  
145 Hydrology controls the water available for vegetation. The hydrology submodule in ED tracks soil moisture  
146 dynamics between incoming water flow from precipitation and outgoing flow through percolation, runoff, and  
147 transpiration. Previous ED versions did not include evaporation from soil and canopy and also did not account for  
148 snow dynamics. Here, evaporation from soil and canopy is estimated based on the Penman-Monteith (P-M) equation  
149 (Monteith, 1965; Mu et al., 2011). In addition, a simple snow dynamics process is introduced to decrease water  
150 availability for plants when air temperature drops below the freezing point and increase it when air temperature rises  
151 above freezing point at a rate depending on air temperature. More details can be found in Supplement S9.

152  
153 Land use activities (e.g., deforestation and wood harvesting) remove vegetation carbon from ecosystems for various  
154 purposes. This carbon is traditionally tracked in wood product pools, with different lifetimes and temporal emissions  
155 to the atmosphere. The previous land use submodule in ED only tracked changes in vegetation and soil carbon  
156 during various land use activities but did not track subsequent decay process of product pools (Hurtt et al., 2002). In  
157 ED v3.0, three wood product pools are added to track the life cycles of harvested wood and associated decay  
158 processes (Supplement S11). Wood product pools gain carbon from land use activities such as wood harvesting or  
159 deforestation, and lose carbon through decay and emissions to the atmosphere. The loading of these product pools,  
160 and their decay rates, are based on a prior study (Hansis et al., 2015).

## 161 **2.2 Model initialization**

162 Global spin-up of ED initialized ecosystems to contemporary conditions by taking into account climate change,  
163 rising CO<sub>2</sub> and land use change. The global spin-up was comprised of two separate runs at 0.5° spatial resolution.  
164 The first run, called the “equilibrium simulation”, ran ED from initial conditions to equilibrium. This run was  
165 performed for 1000 years by which time PFT composition and carbon pools of vegetation and soil reached a  
166 dynamic equilibrium. The second run, called “transient simulation”, restarted from the end of the equilibrium  
167 simulation and simulated for 1166 years, corresponding to the period A.D. 851 – A.D. 2016, with varying CO<sub>2</sub>  
168 levels, land-use change, and climate variability. Both runs were driven with meteorological forcing from NASA  
169 Modern-Era Retrospective analysis for Research and Applications, version 2 (MERRA2) (Gelaro et al., 2017) and  
170 surface CO<sub>2</sub> concentration from NOAA CarbonTracker Database, version 2016 (NOAA CT2016) (Peters et al.,  
171 2007, with updates documented at <http://carbontracker.noaa.gov>). Additionally, the transient simulation run utilized  
172 prescribed burned area from the Global Fire Emissions Database, version 4 (GFED4) (Randerson et al., 2015) and  
173 forced land-use change from Land Use Harmonization, version 2 (LUH2) (Hurtt et al., 2019b, 2020). Details of  
174 these simulations are provided below.



175

176 The equilibrium simulation was started from bare ground where the soil and vegetation carbon pools were set at  
177 zero, and all PFTs were initialized with equal seedling density for all patches and all grid cells over the globe. This  
178 run was driven for 1000 years with MERRA2 climatology of 1981-1990 and NOAA CT2016 average surface CO<sub>2</sub>  
179 between 2001-2014 (with spatial variation and global average rescaled to 280 ppm). No climatic envelope or  
180 potential biome maps were used to constrain PFT spatial distribution; competition determined final PFT  
181 distributions, vegetation structure, and carbon stocks. The land-use change module was disabled in this run of  
182 simulation.

183

184 The transient simulation was restarted from equilibrium conditions. The land-use change submodule was activated,  
185 and all land-use transition types from LUH2 were incorporated into the simulation at annual time steps. These  
186 transitions included changes in agriculture and forest extent, shifting cultivation, and wood harvesting, among  
187 others. MERRA2, NOAA CT2016 and GFED were used throughout the simulation with varying temporal settings  
188 depending on data availability. Specifically, for MERRA2, a climatology between 1981-1990 was used until 1981,  
189 and annual meteorology was used subsequently. For NOAA CT2016, an average surface CO<sub>2</sub> concentration between  
190 2001-2014, which varies spatially and grows over time, was used until 2000, while annual NOAA CT2016 surface  
191 CO<sub>2</sub> concentrations were used subsequently. For GFED4 burned area, an average between 1996-2016 was used until  
192 1996, after which annual burned area was used.

### 193 **2.3 Forcing data**

194 Meteorological variables utilized from MERRA2 include surface air temperature (TLML), surface specific humidity  
195 (QLML), precipitation (PRECTOTCORR), incident shortwave radiation (SWGDN), surface wind speed (SPEED),  
196 and multi-layer soil temperature (TSOIL1-TSOIL3). Original estimates of surface air temperature, surface specific  
197 humidity, incident shortwave radiation, and surface wind speed were averaged from daily hourly to monthly hourly  
198 for each year between 1981 to 2016. The resulting annual monthly average of diurnal meteorological variables were  
199 used to drive the leaf physiology submodule in ED. Hourly surface air temperature, precipitation, and soil  
200 temperature were also aggregated to monthly averages for each year between 1981 to 2016, and then used to drive  
201 the soil hydrology, phenology, evapotranspiration, and biogeochemical modules in ED.

202

203 Surface CO<sub>2</sub> concentration was extracted from the lowest vertical level of NOAA CT2016 CO<sub>2</sub> mole fraction which  
204 is temporally and spatially varying. The original datasets were first linearly interpolated from 3°x2° (longitude x  
205 latitude) to 0.5°x0.5° and from 3-hour to hourly, and then averaged to monthly hourly estimates for each grid cell  
206 and each year between 2001 and 2014, resulting in surface CO<sub>2</sub> concentration maps with 4032 timesteps (14 years,  
207 24 hours, 12 months) for each 0.5°x0.5° grid. The surface CO<sub>2</sub> concentration maps were used to drive the transient  
208 simulation from 850 to 2000, retaining average spatial variation between 2001 and 2014 and applying a scaling  
209 factor to force the global annual average CO<sub>2</sub> concentration to remain at 280 ppm before 1850, then grow linearly to



210 310 ppm in 1950 and to 375 ppm in 2000. This increasing trend in global average matches observed CO<sub>2</sub> growth  
211 rates from Keeling (2008).

212

213 LUC forcing was derived from the LUH2 (version v2h) for years 850-2015 (Hurtt et al., 2019b, 2020). The original  
214 land use state and land use transitions were aggregated from a spatial resolution of 0.25°x0.25° to 0.5°x0.5° for each  
215 year between 850 and 2015. Subtypes of land use states and associated transitions were grouped into the major land  
216 use types of the model's predecessor version (LUH1). Specifically, sub crop types of C3 annual crops (c3ann), C3  
217 perennial crops (c3per), C4 annual crops (c4ann), C4 perennial crops (c4per) and C3 nitrogen-fixing crops (c3nfx)  
218 were all merged as cropland. Forested primary land (primf) and non-forested primary land (primn) were merged as  
219 primary land; forested secondary land (secdf) and non-forested secondary land were merged as secondary land; and  
220 managed pasture (pastr) and rangeland were merged as pasture. Note that all types of land use transitions and gross  
221 transition rate were used in ED's land use module.

222

223 Soil properties, including depth, hydraulic conductivity, and residual and saturated volumetric water content are  
224 important for determining plant water availability. These soil properties were taken from Montzka et al. 2017.  
225 Additional details can be found in the supplement (S9, hydrology submodule).

## 226 **2.4 Model evaluation**

227 A benchmarking package of data (Table 1) was collected to evaluate ED performance. Eight critical variables were  
228 assessed in four categories including: PFT distribution, carbon stocks in vegetation and soil, carbon and water  
229 fluxes, and vegetation structures in terms of canopy height and vertical LAI. Evaluation was carried out at different  
230 spatial (grid, latitudinal, and biome) and temporal scales (climatological, seasonal, and interannual). For each  
231 variable, a widely used dataset was used for reference, and in some cases, these span different years. An important  
232 feature of our method was to adjust the simulation years from ED to match each benchmarking dataset.

### 233 **2.4.1 Vegetation distribution**

234 The satellite-based land cover product, ESA CCI, was used to examine the distribution of three modelled PFTs,  
235 grass, broadleaf trees, and needleleaf trees (ESA 2017). Many satellite-based land cover datasets differ largely from  
236 ED in PFT definition. For example, no successional PFTs exist in ESA CCI land cover types. Thus, the native PFTs  
237 in ED and ESA CCI both have to be aggregated to broader categories such as broadleaf PFTs, needleleaf PFTs, and  
238 grass PFTs. To do this, the 22 native land cover classes of ESA CCI were first reclassified to 'broadleaf evergreen  
239 tree', 'broadleaf deciduous tree', 'needleleaf evergreen tree', 'needleleaf deciduous tree', 'natural grass' and  
240 'manned grass' using a cross-walk table (Poulter et al., 2015). They were then further merged by phenology type  
241 and aggregated to 0.5°, resulting in PFT fraction maps of broadleaf PFTs, needleleaf PFTs, and grass and shrub  
242 PFTs. ED PFTs of EaSBT, MiSBT and LaSBT were merged as broadleaf PFTs, NSP and LaSC were merged as  
243 needleleaf PFTs, and C3ShG and C4ShG were merged as grass and shrub PFTs.



#### 244 **2.4.2 Carbon fluxes**

245 Evaluation of carbon fluxes focused on GPP and NBP. Modelled GPP was evaluated with respect to spatial pattern,  
246 seasonality, and interannual variability using two satellite data-driven GPP datasets, FLUXCOM (Jung et al., 2020)  
247 and FluxSat (Joiner et al., 2018), and the satellite-retrieved sun-induced chlorophyll fluorescence (CSIF) dataset  
248 (Zhang et al., 2018). The FLUXCOM and FluxSat datasets are derived from a data-driven approach that combines  
249 carbon fluxes measurements from FLUXNET and satellite observations from MODIS. Major differences between  
250 FLUXCOM and FluxSat include the use of meteorological forcing and the specific approach used. FLUXCOM used  
251 meteorological forcing and a machine learning approach, while FluxSat used a simplified light-use efficiency model  
252 that does not rely upon meteorological forcing. FluxSat also used satellite-based sun-induced chlorophyll  
253 fluorescence (SIF) to delineate highly productive regions. Satellite measurements of SIF have recently been  
254 suggested as a promising proxy of terrestrial GPP, exhibiting high sensitivity to plant photosynthetic activities (Lee  
255 et al., 2013; Guanter et al., 2014; Yang et al., 2015). In this study, we chose the CSIF dataset for its improved  
256 spatiotemporal continuity. CSIF is generated by fusing Orbiting Carbon Observatory-2 (OCO-2)-retrieved SIF and  
257 MODIS reflectance data using a machine learning approach. FLUXCOM, FluxSat, and CSIF were all resampled to  
258 monthly estimates at 0.5x0.5 spatial resolution before the evaluation.

259  
260 Modelled net biome productivity (NBP) was compared against multiple sources including estimates from process-  
261 based models, atmospheric inversions, and the 2020 global carbon budget (GCB2020) (Friedlingstein et al., 2020).  
262 For process-based models, 17 DGVMs reported in the GCB2020 were used to calculate the respective net land sink  
263 by differencing land uptake and land use emissions estimates (i.e.,  $S_{\text{LAND}} - E_{\text{LUC}}$ ). For atmospheric inversions, three  
264 systems are used, namely CarbonTracker Europe (CTE) (van der Laan-Luijkx et al., 2017), Jena CarboScope  
265 (version s81oc) (Rödenbeck et al., 2008) and the Copernicus Atmosphere Monitoring Service (CAMS) (Chevallier  
266 et al., 2005). The three inversions all derive surface carbon fluxes using atmospheric CO<sub>2</sub> measurements, prior  
267 constraints on fluxes, and an uncertainty and atmospheric transport model, but vary with respect to the specific data,  
268 prior constraints, and transport models used (Peylin et al., 2013). In the GCB2020, the residual terrestrial sink was  
269 used, which was calculated as total emissions from fossil fuel and land use change minus the atmospheric CO<sub>2</sub>  
270 growth rate and ocean sink (i.e.,  $E_{\text{FF}} + E_{\text{LUC}} - G_{\text{ATM}} - S_{\text{OCEAN}}$ ).

#### 271 **2.4.3 Carbon stocks**

272 Modelled carbon pools were evaluated with regards to vegetation aboveground biomass (AGB) and soil carbon. The  
273 reference AGB data included estimates from Santoro et al. (2018) and Spawn et al. (2020). These two AGB datasets  
274 provide high spatial resolution (e.g., 100 m to 1000 m) wall-to-wall global estimates of the year 2010, but differ in  
275 their methodologies. Specifically, AGB from Santoro et al. (2018) was produced by combining spaceborne synthetic  
276 aperture radar (SAR) (ALOS PLASAR, Envisat ASAR), Landsat-7, and Lidar observations from Ice, Cloud, and  
277 land Elevation Satellite (ICESat). AGB from Spawn et al. (2020) includes biomass of forests and also other woody  
278 non-forest plants. Reference soil carbon was from the Harmonized World Soil Database (HWSD) (Wieder et al.,  
279 2014), including soil carbon for topsoil (0 to 30 cm) and subsoil (30 to 100 cm).



#### 280 **2.4.4 Vegetation structure**

281 Evaluation of modelled forest structure focused on total and vertical distribution of leaf area index (LAI) and tree  
282 canopy height. Two reference LAI products, namely MODIS MCD15A3H (Myneni et al., 2015) and GEOV2 LAI  
283 (Verger et al., 2014), are used for evaluating total LAI in terms of spatial distribution, seasonality, and interannual  
284 variability. The MODIS and GEOV2 LAI datasets were both derived from passive optical observations with  
285 empirical-based inversion methods which relate leaf area with optical canopy reflectance or vegetation indices;  
286 however, these two products vary with source of optical observations and choices for inversion methods. Reference  
287 vertical LAI was from the Global Ecosystem Dynamics Investigation (GEDI) L2B products, which retrieves leaf  
288 vertical distribution from lidar waveform return (Dubayah et al., 2020b). Reference canopy height data were based  
289 on direct forest structure observations from GEDI L2A (Dubayah et al., 2020c) and the ICESat-2 ATL08 products  
290 (Neuenschwander et al., 2020). Mean canopy height was generated at 0.5° spatial resolution from the relative height  
291 98<sup>th</sup> percentile (RH98) of all GEDI L2A footprints and canopy top height (h<sub>canopy</sub>) of all ICESat-2 ATL08  
292 segments of good quality.

### 293 **3 Results**

294 ED results were evaluated across four primary categories: PFT distribution, vegetation and soil carbon pools, carbon  
295 and water fluxes, and vegetation structure. Evaluation included comparing modelled global quantities, and their  
296 associated spatial and temporal patterns, to the benchmarking datasets.

#### 297 **3.1 Evaluation of PFT distribution**

298 Global total area of broadleaf PFTs, needleleaf PFTs and grass and shrub PFTs were estimated by ED to be 24.30,  
299 8.93 and 24.63 million km<sup>2</sup> respectively. These results compare to ESA CCI data which estimate the same  
300 respective global PFT areas at 20.13, 10.65 and 41.49 million km<sup>2</sup>. The global spatial distribution and corresponding  
301 zonal distribution of broadleaf PFTs, needleleaf PFTs and grass and shrub PFTs are shown in Fig. 3. In this  
302 comparison, the major patterns of ED estimated PFT distribution were similar to the observed distribution of PFTs.  
303 ED estimated needleleaf PFTs were dominate at high latitudes, broadleaf PFTs dominated in the tropics, and grass  
304 and shrub PFTs were widespread globally. ED also predicted the observed coexistence of broadleaf and needleleaf  
305 PFTs in southern China and eastern US. However, beyond these major patterns, ED estimates differed in some  
306 specific regions. For example, ED predicted the existence of needleleaf PFTs along the Andes Mountains in South  
307 America and in southern Australia. While this pattern was not evident in the ESA CCI data, there are other studies  
308 based on ground observations that support it (Farjon and Filer, 2013). ED also estimated relatively more broadleaf  
309 PFTs in eastern Europe and southern China, less broadleaf PFTs in Africa savanna, less needleleaf PFTs in east  
310 Siberia, and less grass and shrub PFTs both in Africa savanna and northern China. Analogous results can also be  
311 seen zonally, where major patterns of PFTs are broadly similar to observed but with some specific differences. In  
312 terms of zonal distribution per PFT, the smallest discrepancies between ED and ESA CCI appear in broadleaf PFTs,  
313 followed by needleleaf PFTs, and grass and shrub PFTs.



### 314 3.2 Evaluation of AGB and soil carbon

315 ED estimates of AGB were compared to corresponding benchmark data. ED estimated global total aboveground  
316 vegetation carbon (including forest and non-forest) at 298 Pg C in 2010. This compares to 283 Pg C and 297 Pg C  
317 estimated by Spawn et al. (2020) and Santoro et al. (2018). ED's estimate of the spatial pattern of AGB was also  
318 comparable to that of both two benchmark datasets, with the highest biomass densities across the tropics (i.e., the  
319 Amazon rainforest, the Congo river basin, and southeast Asia) with declining biomass densities northward towards  
320 the temperate and boreal regions. For example, similar to observations, average estimated AGB density was ~15 kg  
321 C/m<sup>2</sup> in the tropics and less than 2.5 kg C/m<sup>2</sup> across temperate and boreal regions (Fig. 4d). In addition, the AGB  
322 transition along the African forests-savanna zone was represented by ED, albeit with lower values in the savanna.  
323 Major discrepancies between ED and benchmarking data appear in southern China, southeast Asia and southeast  
324 Brazil.

325

326 ED estimates of soil carbon were compared to benchmark data on soil carbon. ED estimated total global soil carbon  
327 at 671 Pg C in 2000, which was within the range of CMIP5 ESMs (510 - 3040 Pg C) (Todd-Brown et al., 2013), but  
328 lower than the HWSD estimate of 1201 Pg C. Comparing total stocks at the biome level (Fig. 5d) showed that ED  
329 generally reproduced soil carbon variation across biomes, but notably underestimated carbon in boreal forest/taiga,  
330 deserts and xeric shrublands, tropical and subtropical grasslands, savannas and shrubland. The soil carbon map from  
331 ED revealed different spatial patterns compared to HWSD, with relatively less spatial heterogeneity and fewer  
332 regions with densities above 30 kg C/m<sup>2</sup>.

### 333 3.3 Evaluation of GPP, NBP and ET

334 Globally, the ED estimate of average annual GPP was 134 Pg C yr<sup>-1</sup> between 2001-2016, which compares to 120 Pg  
335 C yr<sup>-1</sup> from FLUXCOM and 136 Pg C yr<sup>-1</sup> from FluxSat over the same period. The spatial pattern of GPP from ED  
336 was also compared to benchmark values at the grid and latitudinal scales (Fig. 6). Similar to observations, areas of  
337 highest productivity occur in the tropics, followed by temperate and boreal regions. For the tropics, ED was ~0.5 kg  
338 C/m<sup>2</sup>/yr higher than FLUXCOM, and ~0.2 kg/C/m<sup>2</sup> higher than FluxSat, but lower than both over the Africa  
339 Savanna. Additionally, ED was relatively higher in southern China and Brazil than either benchmark dataset. A  
340 notably increasing annual trend in total global GPP can be seen in both ED and FluxSat estimates between 2001-  
341 2016 as well as from globally averaged CSIF (Fig. 7). ED also reproduced GPP interannual variability from FluxSat,  
342 FLUXCOM and CSIF, dipping in the years 2005, 2012 and 2015, and peaking in 2006, 2011 and 2014. Regarding  
343 latitudinal seasonality at the biome scale (Fig. 8), ED captured GPP timing for most latitudinal zones including 60° -  
344 90°N, 45° - 60°N, 15° - 30°N and 60° - 30°S. Major differences appear in 30° - 45°N, where ED shows decreases  
345 from July-September, and in 15°S - 0°, where ED shows delayed monthly timing of lowest annual GPP values.

346

347 Globally, the ED estimate of average annual NBP between 1981 and 2016 was 1.99 Pg C/yr, which can be  
348 compared to 1.21-1.80 Pg C/yr from atmospheric inversions, 1.11 Pg C/yr from DGVMs, and 1.31 Pg C/yr from  
349 GCB2020 residual terrestrial sink. ED estimates were also compared to benchmark datasets on global changes over



350 time (Fig. 9). Similar to the references, ED estimated an increasing trend with substantial interannual variation  
351 during the 1981-2015 period. This variation included reductions in El Niño years (such as 1983, 1998 and 2015) and  
352 increases in La Niña years (such as 1989, 2001-2002 and 2011). An exception is 1991-1992, where ED and DGVMs  
353 were both lower than atmospheric inversions. This period includes the Mt. Pinatubo eruption the effect of which is  
354 not included in the shortwave radiation forcing of GCB2020 DGVMs or ED (Mercado et al., 2009; Friedlingstein et  
355 al., 2020). During the period 2007-2016, ED produced a continued increasing trend over the 2007-2016 period as  
356 reflected in the mean of atmospheric inversions, but not the mean of DGVMs. Specifically, ED estimated NBP  
357 averaged 2.34 Pg C/yr from 2007-2016, which is within the range of the atmospheric inversions estimates (1.77 -  
358 2.64 Pg C/yr) and DGVMs estimates (0.58 - 2.82 Pg C/yr), but higher than either the mean of DGVMs (1.40 Pg  
359 C/yr) or the GCB2020 residual terrestrial sink (1.81 Pg C/yr). Despite the similarities in global trends, the latitudinal  
360 comparison between ED and atmospheric inversions indicated contrasting attribution of the global sink (Fig. 10). In  
361 comparison to the atmospheric inversions, ED predicted a stronger sink in tropics and relatively weaker sink in the  
362 Northern Hemisphere. Such a pattern was highlighted in the global carbon budget (Friedlingstein et al., 2020),  
363 where process-based models and the atmospheric inversions generally show less agreement on the spatial pattern of  
364 the carbon sink in these two regions. There is recognized uncertainty about the underlying actual pattern due in part  
365 to the in-situ network, which is spatially biased towards the mid-latitudes (i.e., more observational sites) relative to  
366 the tropics (i.e., fewer observational sites) (Ciais et al., 2014b).

367

368 Globally, the ED estimate of global mean annual ET between 1981 and 2014 was 393.46 mm/yr, which can be  
369 compared to 582.10 mm/yr from FLUXCOM. ED estimates of ET were also compared to gridded FLUXCOM data  
370 and by latitude (Fig. 11). Similar to the reference dataset, ED estimated the highest rates across the tropics with  
371 decreases towards high latitudes. This pattern generally followed the spatial distribution of precipitation. ED estimates  
372 were close to FLUXCOM over the tropics (i.e., 1500 mm/yr) as well as latitudes above 60°N and below 35°S (i.e.,  
373 below 500 mm/yr), but notably underestimated average annual ET in other latitudes. ED estimates were generally  
374 smaller than FLUXCOM in dry regions such as southern Africa and interior Australia.

### 375 **3.4 Evaluation of canopy height and LAI vertical profile**

376 Evaluation of vegetation structure estimates focused on leaf area and canopy height. Fig. 12 presents the spatial  
377 distribution of growing season LAI from ED, GEOV2, and MODIS. Growing season LAI is chosen for comparison  
378 because winter snow in the northern region (e.g., boreal forests) might affect LAI retrieval and cause uncertainties in  
379 remote sensing estimates (Murray-Tortarolo et al., 2013). There was good agreement in spatial pattern between ED  
380 and reference LAIs (Fig. 12d), showing peaks in the tropics and boreal region (near 50°N), and relatively low  
381 estimates across temperate regions. In the tropics, ED estimated an average LAI of 6.0 m<sup>2</sup>/m<sup>2</sup>, which was similar to  
382 GEOV2 but higher than MODIS. However, ED produced higher LAI in temperate and boreal regions than both  
383 reference datasets, specifically in southern China and Brazil. Despite these differences there was a general  
384 agreement in the greening trend between 1999 and 2016 (as shown in Fig. 13). The linear fitted LAI trend was 0.058  
385 m<sup>2</sup>/m<sup>2</sup> per decade for ED, 0.090 m<sup>2</sup>/m<sup>2</sup> for GEOV2 and 0.046 m<sup>2</sup>/m<sup>2</sup> for MODIS. LAI seasonality was also



386 compared across latitudinal bands in Fig. 14. Similar to references, ED captured peak season in latitudinal bands 60°  
387 - 90°N, 45° - 60°N, and 60° - 30°S, but shows less agreement with the references in the tropics (0° - 15°N and 15S°  
388 - 0°). In addition, ED LAI in winter is larger than either reference LAI; at latitudes above 45°N, and between 30°N  
389 and 45°N, ED LAI is higher for all seasons. Similarly, higher LAI also appears in 60°S - 30°S, across southern  
390 China and Brazil.

391

392 The estimated vertical profile of LAI from ED was compared to GEDI both spatially and by latitude band. Spatially,  
393 ED and GEDI L2B had a similar spatial pattern with most vegetated regions having concentrated LAI under 10m,  
394 and only tropical forests, part of southern China and the US having substantial LAI above 30m (Fig. 15).

395 Comparisons of LAI profiles by latitude band indicate close agreement in each zone, and with all regions having the  
396 highest values of LAI closest to the ground (0-5 m) and decreasing with canopy height (Fig. 16). Discrepancies can  
397 be seen at the 0 - 5m and 10 - 15m LAI interval along most latitudinal bands, where ED tends to be higher 0-5m,  
398 and lower in the 10-15m bin.

399

400 Tree canopy height estimates from ED were compared with satellite lidar observations from GEDI and ICESat-2  
401 (Fig. 17). Like the reference datasets, ED produced a spatial pattern with taller trees in tropical rainforests, southern  
402 China and the eastern US. The canopy height gradient from forests to savannas in South America (northwest to  
403 southeast) and in Africa (central to north and south) were also generally captured by ED. Latitudinal comparison  
404 shows ED estimated average height is above 30 m in tropics and is ~10m in temperate regions. The general  
405 differences between ED and reference datasets are less than 10m across all latitudes. However, ED tree height in  
406 southern China and Brazil was higher than the references, and lower than references across African savanna.

#### 407 **4 Discussion and Conclusions**

408 In this study, we developed a new global version of the Ecosystem Demography model and evaluated it against  
409 benchmark datasets for a wide range of important variables spanning carbon stocks, carbon and water fluxes,  
410 vegetation distribution, and vegetation structure. Historically, different models have been developed separately in  
411 areas of biogeochemistry, biogeography, and biophysics, and in some cases important patterns have been set through  
412 observations or other prior constraints (Bonan, 1994; Dickinson, 1993; Haxeltine and Prentice, 1996; Hurtt et al.,  
413 1998, Lieth, 1975; Neilson, 1995; Parton, 1996; Potter et al., 1993; Prentice et al., 1992; Raich et al., 1991; Sellers et  
414 al., 1986). The ability of this model to reliably simulate such a wide range of phenomena globally in a single  
415 mechanistic and consistent framework represents an important interdisciplinary synthesis, a functional modelling  
416 advance, and to our knowledge is unprecedented.

417

418 ED estimation of carbon stocks and fluxes compared favourably to benchmarking datasets across a range of spatial  
419 and temporal scales, from grid cell to global, from seasonal to decadal. Similar to benchmarking datasets, ED  
420 produced latitudinal gradients of GPP and AGB, positive trend in global total GPP, global total AGB and GPP  
421 within reference range, and interannual variation of NBP in response to El Niño and La Niña events. Producing such



422 patterns of both global carbon fluxes and stocks is challenging, as it requires models to have the ability to  
423 mechanistically scaling up physiological processes from leaf to ecosystem scales. It also requires models to  
424 accurately characterize responses of ecosystem demographic processes to climate change, soil conditions, and land  
425 use activities. As a part of a new generation of DGVMs attempting to meet these challenges, ED leverages advances  
426 in detailed understanding of ecosystem-physiology (e.g., Ball–Berry stomatal conductance model and Farquhar  
427 photosynthesis model) (Ball et al., 1987; Farquhar 1980), soil biogeochemistry (e.g., CENTURY soil model) (Parton  
428 1996), and processes of disturbance and recovery (e.g., LUH1/LUH2 modelling of land-use transition through time)  
429 (Hurtt et al., 2011, 2020). This study is the first, to our knowledge, to combine ecosystem demography and land use  
430 history to simulate global carbon dynamics and compare to a wide range of benchmarks.

431  
432 In addition to carbon stocks and fluxes, ED simultaneously estimated the spatial distribution of the major PFTs  
433 globally. ED produced dominance of broadleaf PFT in tropics and needleleaf PFT in high latitudes, which is similar  
434 to benchmarking data. The ability to estimate these patterns mechanistically required the ability to characterize  
435 functional plant traits and trade-offs of vegetation as well as the processes and timescales of competition for light,  
436 water, and other resources. Numerous studies have made previous advances which contributed to the progress in this  
437 study. For example, plant traits have been observed and compiled crossing a wide range species and geographical  
438 domain (Reich 1997 et al., 1997; Kattge et a., 2011, 2020). Individual based/gap models have been developed to  
439 track the life cycle of each individual tree and competition between individuals on plot and site level (Botkin et al.,  
440 1972; Shugart and West 1977; Shugart et al., 2018; Pacala et al., 1996). Meanwhile, the SAS scaling approach was  
441 previously developed to efficiently scale up the individual scale to ecosystem dynamics at regional and continental  
442 scales (Hurtt et al., 1998; Moorcroft et al., 2001).

443  
444 ED estimation of vegetation structure was also evaluated against benchmark data, in this case, novel observations  
445 using lidar remote sensing. Impressively, ED mechanistically and independently produced latitudinal mean height  
446 and LAI profiles similar to benchmarking datasets on vegetation structure. This progress is perhaps the most novel  
447 achievement because progress on this topic was previously limited due to lack of global observations of vegetation  
448 structure. Importantly, the ED model is natively height-structured, in that all trees have explicit height. Originally,  
449 this feature was included to enable simulation of individual-based competition for light. This feature however also  
450 offers the potential for direct connection to lidar observations on vegetation structure for the purpose of model  
451 validation and/or initialization. Numerous studies have been completed at local and regional scales by initializing  
452 the ED model with airborne lidar data, demonstrating the power of lidar technique in improving characterization of  
453 contemporary ecosystems conditions (Hurtt et al., 2004, 2010, 2016, 2019a and Ma et al., 2021). The advent of  
454 GEDI (Dubayah et al., 2020a) and ICESat-2 (Markus et al., 2017) has now expanded the potential for model  
455 evaluation and initialization to global scales.

456  
457 Despite all of these advances, no model is perfect. There are important examples of differences between ED  
458 estimates and reference values that present important challenges for the future. Two examples are important to



459 consider further. First, ED estimates of AGB/GPP exceeded reference values in some regions, most notably southern  
460 China, southeast Asia and southeast Brazil. Correspondingly, ED also tended to overestimate tree height in these  
461 same regions. The discrepancies share a similar spatial pattern and are likely interrelated. One hypothesis is that this  
462 overestimation may result at least in part from the land-use forcing. The LUH2 has been shown to underestimate  
463 harvesting area on primary forest in southern China, and Southeast Asia for the period after 1950, and also  
464 underestimates total cropland area in Brazil (Chini et al., 2021). LUH2 is being continuously updated and improved  
465 through the contribution to the Global Carbon Budget project (Chini et al., 2021). Second, while relative patterns for  
466 soil carbon showed close agreement at biome level for the majority of biomes, the absolute magnitude of soil carbon  
467 was much lower than reference for several biomes and thus globally. Before over-interpreting these differences, it  
468 should be noted that there are substantial uncertainties with current empirical soil carbon maps in terms of both  
469 global totals and spatial distribution (Todd-Brown et al., 2013). Model errors in soil carbon may arise from poor  
470 representations of biophysical conditions, inaccurate parameterization, or lack of other important drivers. Soil  
471 carbon representation in ED, like that of many other DGVMs/ESMs, is highly simplified and strongly driven by  
472 NPP and soil temperature, but these two drivers have been shown to only explain a small amount of spatial variation  
473 in the HWSD map (Todd-Brown et al., 2013). The underestimation in the boreal forest/Taiga biome in particular is  
474 likely due to a combination of these factors. Ongoing research through the NASA Arctic-Boreal Vulnerability  
475 Experiment (ABOVE) program and the Next-Generation Ecosystem Experiments (NGEE Arctic) program will likely  
476 improve both the data and model parameterization in this critical region.

477

478 Previous studies have developed benchmarking packages and designed model intercomparison activities to evaluate  
479 model performance (Abramowitz et al., 2012; Collier et al., 2018; Eyring et al., 2016; Ghimire et al., 2016; Kelly et  
480 al., 2013; Luo et al., 2012; Randerson et al., 2009; Sitch et al., 2008). Like those studies, we evaluated ED model  
481 results using many key datasets and variables. The work here has utilized a particularly wide range of variables,  
482 utilized the latest versions of key forcing data on climate and land-use, and added a new focus on vegetation  
483 structure.

484

485 Future work will focus on addressing the limitations discussed above and making direct connections with lidar forest  
486 structure observations from GEDI and ICESat-2 to improve demographic processes, and the quantification and  
487 attribution of the terrestrial carbon cycle. Meanwhile, the global development and evaluation of ED demonstrates the  
488 model's ability to characterize essential aspects of terrestrial vegetation dynamics and the carbon cycle for a range of  
489 important applications. This model has recently been integrated with NASA's Goddard Earth Observing System,  
490 Version 5 (GEOS-5) to forecast seasonal biosphere-atmosphere CO<sub>2</sub> fluxes in 2015-16 El Niño (Ott et al., 2018),  
491 and used in NASA Carbon Monitoring System as the tool for high spatial resolution (e.g., 90 m) regional forest  
492 carbon modelling and monitoring (Hurt et al., 2019a; Ma et al., 2021), and also by NASA Global Ecosystem  
493 Dynamics Investigation mission for quantification of land carbon sequestration potential (Dubayah et al., 2020a; Ma  
494 et al., 2020). Results from these studies will likely be of importance to science applications, and also be used to  
495 inform and prioritize future model advances. Meanwhile, the increasing number of remote sensing missions and



496 related data sets, advances in computation, and growing stakeholder interests in carbon and climate, as evidenced by  
497 the Paris Agreement, bode well for future advances.

498

499 *Code and data availability.* All model simulation and source script can be found in  
500 <https://doi.org/10.5281/zenodo.5236771>. All benchmarking datasets are cited and publicly available.

501

502 *Author contributions.* LM, GH, JF, SF and RS developed model code. LM, GH and LO designed this study. LM  
503 conducted model simulation and evaluation. LM, GH and RL wrote main body of the manuscript. All authors  
504 contributed to analysis and manuscript preparation.

505

506 *Competing interests.* The authors declare that they have no conflict of interest.

507

508 *Acknowledgements.* This work was funded by NASA-CMS (grant no. 80NSSC17K0710, 80NSSC20K0006, and  
509 80NSSC21K1059), and NASA-IDS (grant no. 80NSSC17K0348).

## 510 **References**

511 Abramowitz, G.: Towards a public, standardized, diagnostic benchmarking system for land surface models, 5, 819–  
512 827, <https://doi.org/10.5194/gmd-5-819-2012>, 2012.

513 Albani, M., Medvigy, D., Hurtt, G. C. and Moorcroft, P. R.: The contributions of land-use change, CO<sub>2</sub> fertilization,  
514 and climate variability to the Eastern US carbon sink, *Global Change Biology*, 12(12), 2370–2390,  
515 <https://doi.org/10.1111/j.1365-2486.2006.01254.x>, 2006.

516 Anav, A., Friedlingstein, P., Kidston, M., Bopp, L., Ciais, P., Cox, P., Jones, C., Jung, M., Myneni, R., and Zhu, Z.:  
517 Evaluating the land and ocean components of the global carbon cycle in the CMIP5 earth system models, 26, 6801–  
518 6843, 2013.

519 Ball, J. T., Woodrow, I. E., and Berry, J. A.: A model predicting stomatal conductance and its contribution to the  
520 control of photosynthesis under different environmental conditions, in: *Progress in photosynthesis research*,  
521 Springer, 221–224, 1987.

522 Beer, C., Reichstein, M., Tomelleri, E., Ciais, P., Jung, M., Carvalhais, N., Rödenbeck, C., Arain, M. A., Baldocchi,  
523 D., Bonan, G. B., Bondeau, A., Cescatti, A., Lasslop, G., Lindroth, A., Lomas, M., Luyssaert, S., Margolis, H.,  
524 Oleson, K. W., Rouspard, O., Veenendaal, E., Viovy, N., Williams, C., Woodward, F. I. and Papale, D.: Terrestrial  
525 Gross Carbon Dioxide Uptake: Global Distribution and Covariation with Climate, *Science*, 329(5993), 834,  
526 <https://doi.org/10.1126/science.1184984>, 2010.

527 Bernacchi, C. J., Singsaas, E. L., Pimentel, C., Jr, A. R. P. and Long, S. P.: Improved temperature response functions  
528 for models of Rubisco-limited photosynthesis, *Plant, Cell & Environment*, 24(2), 253–259,  
529 <https://doi.org/10.1111/j.1365-3040.2001.00668.x>, 2001.

530 Bonan, G. B.: Comparison of two land surface process models using prescribed forcings, 99, 25803–25818, 1994.

531 Botkin, D. B., Janak, J. F. and Wallis, J. R.: Some ecological consequences of a computer model of forest growth,  
532 *The Journal of Ecology*, 849–872, 1972.



- 533 Brovkin, V., Sitch, S., Von Bloh, W., Claussen, M., Bauer, E. and Cramer, W.: Role of land cover changes for  
534 atmospheric CO<sub>2</sub> increase and climate change during the last 150 years, *Global Change Biology*, 10(8), 1253–1266,  
535 <https://doi.org/10.1111/j.1365-2486.2004.00812.x>, 2004.
- 536 von Caemmerer, S. and Furbank, R. T.: Modeling C<sub>4</sub> photosynthesis, *C<sub>4</sub> plant biology*, 173–211, 1999.
- 537 von Caemmerer, S.: *Biochemical models of leaf photosynthesis*, Csiro publishing., 2000.
- 538 von Caemmerer, S., Farquhar, G. and Berry, J.: Biochemical Model of C<sub>3</sub> Photosynthesis, in *Photosynthesis in  
539 silico: Understanding Complexity from Molecules to Ecosystems*, edited by A. Laisk, L. Nedbal, and Govindjee, pp.  
540 209–230, Springer Netherlands, Dordrecht, [https://doi.org/10.1007/978-1-4020-9237-4\\_9](https://doi.org/10.1007/978-1-4020-9237-4_9), , 2009.
- 541 Canadell, J. G., Kirschbaum, M. U. F., Kurz, W. A., Sanz, M.-J., Schlamadinger, B. and Yamagata, Y.: Factoring  
542 out natural and indirect human effects on terrestrial carbon sources and sinks, *Environmental Science & Policy*,  
543 10(4), 370–384, <https://doi.org/10.1016/j.envsci.2007.01.009>, 2007.
- 544 Chevallier, F., Fisher, M., Peylin, P., Serrar, S., Bousquet, P., Bréon, F.-M., Chédin, A. and Ciais, P.: Inferring CO<sub>2</sub>  
545 sources and sinks from satellite observations: Method and application to TOVS data, *Journal of Geophysical  
546 Research: Atmospheres*, 110(D24), <https://doi.org/10.1029/2005JD006390>, 2005.
- 547 Chini, L., Hurtt, G., Sahajpal, R., Frohling, S., Klein Goldewijk, K., Sitch, S., Ganzenmüller, R., Ma, L., Ott, L. and  
548 Pongratz, J.: Land-Use Harmonization Datasets for Annual Global Carbon Budgets, *Earth System Science Data  
549 Discussions*, 1–27, 2021.
- 550 Ciais, P., Sabine, C., Bala, G., Bopp, L., Brovkin, V., Canadell, J., Chhabra, A., DeFries, R., Galloway, J. and  
551 Heimann, M.: Carbon and other biogeochemical cycles, in *Climate change 2013: the physical science basis.  
552 Contribution of Working Group I to the Fifth Assessment Report of the Intergovernmental Panel on Climate  
553 Change*, pp. 465–570, Cambridge University Press, , 2014a.
- 554 Ciais, P., Dolman, A. J., Bombelli, A., Duren, R., Peregon, A., Rayner, P. J., Miller, C., Gobron, N., Kinderman, G.,  
555 Marland, G., Gruber, N., Chevallier, F., Andres, R. J., Balsamo, G., Bopp, L., Bréon, F.-M., Broquet, G., Dargaville,  
556 R., Battin, T. J., Borges, A., Bovensmann, H., Buchwitz, M., Butler, J., Canadell, J. G., Cook, R. B., DeFries, R.,  
557 Engelen, R., Gurney, K. R., Heinze, C., Heimann, M., Held, A., Henry, M., Law, B., Luysaert, S., Miller, J.,  
558 Moriyama, T., Moulin, C., Myneni, R. B., Nussli, C., Obersteiner, M., Ojima, D., Pan, Y., Paris, J.-D., Piao, S. L.,  
559 Poulter, B., Plummer, S., Quegan, S., Raymond, P., Reichstein, M., Rivier, L., Sabine, C., Schimel, D., Tarasova,  
560 O., Valentini, R., Wang, R., van der Werf, G., Wickland, D., Williams, M., and Zehner, C.: Current systematic  
561 carbon-cycle observations and the need for implementing a policy-relevant carbon observing system, 11, 3547–  
562 3602, <https://doi.org/10.5194/bg-11-3547-2014>, 2014b.
- 563 Collatz, G. J., Ball, J. T., Grivet, C., and Berry, J. A.: Physiological and environmental regulation of stomatal  
564 conductance, photosynthesis and transpiration: a model that includes a laminar boundary layer, 54, 107–136, 1991.
- 565 Collatz, G. J., Ribas-Carbo, M., and Berry, J. A.: Coupled photosynthesis-stomatal conductance model for leaves of  
566 C<sub>4</sub> plants, 19, 519–538, 1992.
- 567 Collier, N., Hoffman, F. M., Lawrence, D. M., Keppel-Aleks, G., Koven, C. D., Riley, W. J., Mu, M., and  
568 Randerson, J. T.: The International Land Model Benchmarking (ILAMB) System: Design, Theory, and  
569 Implementation, 10, 2731–2754, <https://doi.org/10.1029/2018MS001354>, 2018.
- 570 Cramer, W., Bondeau, A., Woodward, F. I., Prentice, I. C., Betts, R. A., Brovkin, V., Cox, P. M., Fisher, V., Foley,  
571 J. A., Friend, A. D., Kucharik, C., Lomas, M. R., Ramankutty, N., Sitch, S., Smith, B., White, A. and Young-  
572 Molling, C.: Global response of terrestrial ecosystem structure and function to CO<sub>2</sub> and climate change: results from  
573 six dynamic global vegetation models, *Global Change Biology*, 7(4), 357–373, [https://doi.org/10.1046/j.1365-  
2486.2001.00383.x](https://doi.org/10.1046/j.1365-<br/>574 2486.2001.00383.x), 2001.
- 575 Dickinson, R. E.: Biosphere atmosphere transfer scheme (BATS) version 1e as coupled to the NCAR community  
576 climate model, 1993.



- 577 Dubayah, R., Blair, J. B., Goetz, S., Fatoyinbo, L., Hansen, M., Healey, S., Hofton, M., Hurtt, G., Kellner, J.,  
578 Luthcke, S., Armston, J., Tang, H., Duncanson, L., Hancock, S., Jantz, P., Marselis, S., Patterson, P. L., Qi, W. and  
579 Silva, C.: The Global Ecosystem Dynamics Investigation: High-resolution laser ranging of the Earth's forests and  
580 topography, *Science of Remote Sensing*, 1, 100002, <https://doi.org/10.1016/j.srs.2020.100002>, 2020a.
- 581 Dubayah, R., Tang, H., Armston, J., Luthcke, S., Hofton, M. and Blair, J.: GEDI L2B Canopy Cover and Vertical  
582 Profile Metrics Data Global Footprint Level V001, , [https://doi.org/10.5067/GEDI/GEDI02\\_B.001](https://doi.org/10.5067/GEDI/GEDI02_B.001), 2020b.
- 583 Dubayah, R., Hofton, M., Blair, J., Armston, J., Tang, H. and Luthcke, S.: GEDI L2A Elevation and Height Metrics  
584 Data Global Footprint Level V001, , [https://doi.org/10.5067/GEDI/GEDI02\\_A.001](https://doi.org/10.5067/GEDI/GEDI02_A.001), 2020c.
- 585 Erb, K.-H., Kastner, T., Luysaert, S., Houghton, R. A., Kummerle, T., Olofsson, P. and Haberl, H.: Bias in the  
586 attribution of forest carbon sinks, *Nature Climate Change*, 3(10), 854–856, <https://doi.org/10.1038/nclimate2004>,  
587 2013.
- 588 ESA: Land Cover CCI Product User Guide Version 2. Tech. Rep., Available at:  
589 [maps.elie.ucl.ac.be/CCI/viewer/download/ESACCI-LC-Ph2-PUGv2\\_2.0.pdf](https://maps.elie.ucl.ac.be/CCI/viewer/download/ESACCI-LC-Ph2-PUGv2_2.0.pdf), 2017.
- 590 Farjon, A. and Filer, D.: An Atlas of the World's Conifers: An Analysis of their Distribution, Biogeography,  
591 Diversity and Conservation Status, Brill. <https://brill.com/view/title/20587>, last access: 22 December 2020, 2013.
- 592 Farquhar, G. D., von Caemmerer, S. and Berry, J. A.: A biochemical model of photosynthetic CO<sub>2</sub> assimilation in  
593 leaves of C<sub>3</sub> species, *Planta*, 149(1), 78–90, <https://doi.org/10.1007/BF00386231>, 1980.
- 594 Farquhar, G. D. and Sharkey, T. D.: Stomatal conductance and photosynthesis, 33, 317–345, 1982.
- 595 Fisher, R. A., Muszala, S., Versteinstein, M., Lawrence, P., Xu, C., McDowell, N. G., Knox, R. G., Koven, C., Holm,  
596 J. and Rogers, B. M.: Taking off the training wheels: the properties of a dynamic vegetation model without climate  
597 envelopes, *CLM4. 5 (ED)*, *Geoscientific Model Development*, 8(11), 3593–3619, 2015.
- 598 Fisher, R. A., Koven, C. D., Anderegg, W. R. L., Christoffersen, B. O., Dietze, M. C., Farnior, C. E., Holm, J. A.,  
599 Hurtt, G. C., Knox, R. G., Lawrence, P. J., Lichstein, J. W., Longo, M., Matheny, A. M., Medvigy, D., Muller-  
600 Landau, H. C., Powell, T. L., Serbin, S. P., Sato, H., Shuman, J. K., Smith, B., Trugman, A. T., Viskari, T.,  
601 Verbeeck, H., Weng, E., Xu, C., Xu, X., Zhang, T. and Moorcroft, P. R.: Vegetation demographics in Earth System  
602 Models: A review of progress and priorities, *Global Change Biology*, 24(1), 35–54,  
603 <https://doi.org/10.1111/gcb.13910>, 2018.
- 604 Fisk, J. P.: Net effects of disturbance: Spatial, temporal, and socio-etal dimensions of forest disturbance and recovery  
605 on terrestrial carbon balance, Ph.D thesis, University of Maryland, College Park, Maryland, 2015.
- 606 Fisk, J. P., Hurtt, G. C., Chambers, J. Q., Zeng, H., Dolan, K. A. and Negrón-Juárez, R. I.: The impacts of tropical  
607 cyclones on the net carbon balance of eastern US forests (1851–2000), *Environ. Res. Lett.*, 8(4), 045017,  
608 <https://doi.org/10.1088/1748-9326/8/4/045017>, 2013.
- 609 Flanagan, S. A., Hurtt, G. C., Fisk, J. P., Sahajpal, R., Zhao, M., Dubayah, R., Hansen, M. C., Sullivan, J. H. and  
610 Collatz, G. J.: Potential Transient Response of Terrestrial Vegetation and Carbon in Northern North America from  
611 Climate Change, *Climate*, 7(9), 113, <https://doi.org/10.3390/cli7090113>, 2019.
- 612 Foley, J. A., Prentice, I. C., Ramankutty, N., Levis, S., Pollard, D., Sitch, S., and Haxeltine, A.: An integrated  
613 biosphere model of land surface processes, terrestrial carbon balance, and vegetation dynamics, 10, 603–628, 1996.
- 614 Friedlingstein, P., O'Sullivan, M., Jones, M. W., Andrew, R. M., Hauck, J., Olsen, A., Peters, G. P., Peters, W.,  
615 Pongratz, J. and Sitch, S.: Global carbon budget 2020, *Earth System Science Data*, 12(4), 3269–3340, 2020.
- 616 Gelaro, R., McCarty, W., Suárez, M. J., Todling, R., Molod, A., Takacs, L., Randles, C. A., Darmenov, A.,  
617 Bosilovich, M. G., Reichle, R., Wargan, K., Coy, L., Cullather, R., Draper, C., Akella, S., Buchard, V., Conaty, A.,  
618 da Silva, A. M., Gu, W., Kim, G.-K., Koster, R., Lucchesi, R., Merkova, D., Nielsen, J. E., Partyka, G., Pawson, S.,  
619 Putman, W., Rienecker, M., Schubert, S. D., Sienkiewicz, M. and Zhao, B.: The Modern-Era Retrospective Analysis



- 620 for Research and Applications, Version 2 (MERRA-2), *J. Climate*, 30(14), 5419–5454,  
621 <https://doi.org/10.1175/JCLI-D-16-0758.1>, 2017.
- 622 Guanter, L., Zhang, Y., Jung, M., Joiner, J., Voigt, M., Berry, J. A., Frankenberg, C., Huete, A. R., Zarco-Tejada, P.,  
623 Lee, J.-E., Moran, M. S., Ponce-Campos, G., Beer, C., Camps-Valls, G., Buchmann, N., Gianelle, D., Klumpp, K.,  
624 Cescatti, A., Baker, J. M. and Griffis, T. J.: Global and time-resolved monitoring of crop photosynthesis with  
625 chlorophyll fluorescence, *PNAS*, 111(14), E1327–E1333, <https://doi.org/10.1073/pnas.1320008111>, 2014.
- 626 Hansis, E., Davis, S. J. and Pongratz, J.: Relevance of methodological choices for accounting of land use change  
627 carbon fluxes, *Global Biogeochemical Cycles*, 29(8), 1230–1246, <https://doi.org/10.1002/2014GB004997>, 2015.
- 628 Haxeltine, A. and Prentice, I. C.: BIOME3: An equilibrium terrestrial biosphere model based on ecophysiological  
629 constraints, resource availability, and competition among plant functional types, 10, 693–709, 1996.
- 630 Hurtt, G. C., Moorcroft, P. R., Pacala, S. W. and Levin, S. A.: Terrestrial models and global change: challenges for  
631 the future, *Global Change Biology*, 4(5), 581–590, <https://doi.org/10.1046/j.1365-2486.1998.t01-1-00203.x>, 1998.
- 632 Hurtt, G. C., Pacala, S. W., Moorcroft, P. R., Caspersen, J., Shevliakova, E., Houghton, R. A. and Moore, B.:  
633 Projecting the future of the U.S. carbon sink, *PNAS*, 99(3), 1389–1394, <https://doi.org/10.1073/pnas.012249999>,  
634 2002.
- 635 Hurtt, G. C., Dubayah, R., Drake, J., Moorcroft, P. R., Pacala, S. W., Blair, J. B. and Fearon, M. G.: Beyond  
636 Potential Vegetation: Combining Lidar Data and a Height-Structured Model for Carbon Studies, *Ecological  
637 Applications*, 14(3), 873–883, <https://doi.org/10.1890/02-5317>, 2004.
- 638 Hurtt, G. C., Fisk, J., Thomas, R. Q., Dubayah, R., Moorcroft, P. R. and Shugart, H. H.: Linking models and data on  
639 vegetation structure, *Journal of Geophysical Research: Biogeosciences*, 115(G2),  
640 <https://doi.org/10.1029/2009JG000937>, 2010.
- 641 Hurtt, G. C., Chini, L. P., Frohling, S., Betts, R., Feddema, J., Fischer, G., Fisk, J., Hibbard, K., Houghton, R., and  
642 Janetos, A.: Harmonization of land-use scenarios for the period 1500–2100: 600 years of global gridded annual  
643 land-use transitions, wood harvest, and resulting secondary lands, *Climatic change*, 109, 117–161, 2011.
- 644 Hurtt, G. C., Thomas, R. Q., Fisk, J. P., Dubayah, R. O. and Sheldon, S. L.: The Impact of Fine-Scale Disturbances  
645 on the Predictability of Vegetation Dynamics and Carbon Flux, *PLOS ONE*, 11(4), e0152883,  
646 <https://doi.org/10.1371/journal.pone.0152883>, 2016.
- 647 Hurtt, G. C., Zhao, M., Sahajpal, R., Armstrong, A., Birdsey, R., Campbell, E., Dolan, K., Dubayah, R., Fisk, J. P.,  
648 Flanagan, S., Huang, C., Huang, W., Johnson, K., Lamb, R., Ma, L., Marks, R., O’Leary, D., O’Neil-Dunne, J.,  
649 Swatantran, A. and Tang, H.: Beyond MRV: high-resolution forest carbon modeling for climate mitigation planning  
650 over Maryland, USA, *Environ. Res. Lett.*, 14(4), 045013, <https://doi.org/10.1088/1748-9326/ab0bbe>, 2019a.
- 651 Hurtt, G., Chini, L., Sahajpal, R., Frohling, S., Bodirsky, B. L., Calvin, K., Doelman, J., Fisk, J., Fujimori, S.,  
652 Goldewijk, K. K., Hasegawa, T., Havlik, P., Heinemann, A., Humpenöder, F., Jungclaus, J., Kaplan, J., Krisztin, T.,  
653 Lawrence, D., Lawrence, P., Mertz, O., Pongratz, J., Popp, A., Riahi, K., Shevliakova, E., Stehfest, E., Thornton, P.,  
654 van Vuuren, D., and Zhang, X.: input4MIPs.CMIP6.CMIP.UofMD,  
655 <https://doi.org/10.22033/ESGF/input4MIPs.10454>, 2019b.
- 656 Hurtt, G. C., Chini, L., Sahajpal, R., Frohling, S., Bodirsky, B. L., Calvin, K., Doelman, J. C., Fisk, J., Fujimori, S.  
657 and Klein Goldewijk, K.: Harmonization of global land use change and management for the period 850–2100  
658 (LUH2) for CMIP6, *Geoscientific Model Development*, 13(11), 5425–5464, 2020.
- 659 Jeong, S.-J. and Medvigy, D.: Macroscale prediction of autumn leaf coloration throughout the continental United  
660 States, *Global Ecology and Biogeography*, 23(11), 1245–1254, <https://doi.org/10.1111/geb.12206>, 2014.
- 661 Joiner, J., Yoshida, Y., Zhang, Y., Duveiller, G., Jung, M., Lyapustin, A., Wang, Y. and Tucker, C. J.: Estimation of  
662 Terrestrial Global Gross Primary Production (GPP) with Satellite Data-Driven Models and Eddy Covariance Flux  
663 Data, *Remote Sensing*, 10(9), 1346, <https://doi.org/10.3390/rs10091346>, 2018.



- 664 Jung, M., Schwalm, C., Migliavacca, M., Walther, S., Camps-Valls, G., Koirala, S., Anthoni, P., Besnard, S.,  
665 Bodesheim, P., Carvalhais, N., Chevallier, F., Gans, F., Goll, D. S., Haverd, V., Köhler, P., Ichii, K., Jain, A. K.,  
666 Liu, J., Lombardozi, D., Nabel, J. E. M. S., Nelson, J. A., O'Sullivan, M., Pallandt, M., Papale, D., Peters, W.,  
667 Pongratz, J., Rödenbeck, C., Sitch, S., Tramontana, G., Walker, A., Weber, U. and Reichstein, M.: Scaling carbon  
668 fluxes from eddy covariance sites to globe: synthesis and evaluation of the FLUXCOM approach, *Biogeosciences*,  
669 17(5), 1343–1365, <https://doi.org/10.5194/bg-17-1343-2020>, 2020.
- 670 Kattge, J. and Knorr, W.: Temperature acclimation in a biochemical model of photosynthesis: a reanalysis of data  
671 from 36 species, *Plant, Cell & Environment*, 30(9), 1176–1190, <https://doi.org/10.1111/j.1365-3040.2007.01690.x>,  
672 2007.
- 673 Kattge, J., Bönisch, G., Díaz, S., Lavorel, S., Prentice, I. C., Leadley, P., Tautenhahn, S., Werner, G. D., Aakala, T.,  
674 and Abedi, M.: TRY plant trait database—enhanced coverage and open access, 26, 119–188, 2020.
- 675 Keeling, R. F.: Recording Earth's Vital Signs, *Science*, 319(5871), 1771, <https://doi.org/10.1126/science.1156761>,  
676 2008.
- 677 Keenan, T. F. and Williams, C. A.: The Terrestrial Carbon Sink, *Annu. Rev. Environ. Resour.*, 43(1), 219–243,  
678 <https://doi.org/10.1146/annurev-environ-102017-030204>, 2018.
- 679 van der Laan-Luijckx, I. T., van der Velde, I. R., van der Veen, E., Tsuruta, A., Stanislawski, K., Babenhausenheide,  
680 A., Zhang, H. F., Liu, Y., He, W., Chen, H., Masarie, K. A., Krol, M. C. and Peters, W.: The CarbonTracker Data  
681 Assimilation Shell (CTDAS) v1.0: implementation and global carbon balance 2001–2015, *Geoscientific Model  
682 Development*, 10(7), 2785–2800, <https://doi.org/10.5194/gmd-10-2785-2017>, 2017.
- 683 Lawrence, D. M., Fisher, R. A., Koven, C. D., Oleson, K. W., Swenson, S. C., Bonan, G., Collier, N., Ghimire, B.,  
684 van Kampenhout, L., and Kennedy, D.: The Community Land Model version 5: Description of new features,  
685 benchmarking, and impact of forcing uncertainty, *Journal of Advances in Modeling Earth Systems*, 11, 4245–4287,  
686 2019.
- 687 Lee, J.-E., Frankenberg, C., van der Tol, C., Berry, J. A., Guanter, L., Boyce, C. K., Fisher, J. B., Morrow, E.,  
688 Worden, J. R., Asefi, S., Badgley, G. and Saatchi, S.: Forest productivity and water stress in Amazonia: observations  
689 from GOSAT chlorophyll fluorescence, *Proceedings of the Royal Society B: Biological Sciences*, 280(1761),  
690 20130171, <https://doi.org/10.1098/rspb.2013.0171>, 2013.
- 691 Lieth, H.: Modeling the primary productivity of the world, in: *Primary productivity of the biosphere*, Springer, 237–  
692 263, 1975.
- 693 Longo, M., Knox, R. G., Medvigy, D. M., Levine, N. M., Dietze, M. C., Kim, Y., Swann, A. L. S., Zhang, K.,  
694 Rollinson, C. R., Bras, R. L., Wofsy, S. C. and Moorcroft, P. R.: The biophysics, ecology, and biogeochemistry of  
695 functionally diverse, vertically and horizontally heterogeneous ecosystems: the Ecosystem Demography model,  
696 version 2.2 – Part 1: Model description, *Geoscientific Model Development*, 12(10), 4309–4346,  
697 <https://doi.org/10.5194/gmd-12-4309-2019>, 2019a.
- 698 Longo, M., Knox, R. G., Levine, N. M., Swann, A. L. S., Medvigy, D. M., Dietze, M. C., Kim, Y., Zhang, K.,  
699 Bonal, D., Burban, B., Camargo, P. B., Hayek, M. N., Saleska, S. R., da Silva, R., Bras, R. L., Wofsy, S. C. and  
700 Moorcroft, P. R.: The biophysics, ecology, and biogeochemistry of functionally diverse, vertically and horizontally  
701 heterogeneous ecosystems: the Ecosystem Demography model, version 2.2 – Part 2: Model evaluation for tropical  
702 South America, *Geoscientific Model Development*, 12(10), 4347–4374, <https://doi.org/10.5194/gmd-12-4347-2019>,  
703 2019b.
- 704 Luo, Y. Q., Randerson, J. T., Friedlingstein, P., Hibbard, K., Hoffman, F., Huntzinger, D., Jones, C. D., Koven, C.,  
705 Lawrence, D., and Li, D. J.: A framework for benchmarking land models, 2012.
- 706 Ma, L., Hurtt, G., Ott, L., Sahajpal, R., Fisk, J., Flanagan, S., Poulter, B., Liang, S., Sullivan, J. and Dubayah, R.:  
707 Global Ecosystem Demography Model (ED-global v1.0): Development, Calibration and Evaluation for NASA's



- 708 Global Ecosystem Dynamics Investigation (GEDI), Earth and Space Science Open Archive,  
709 <https://doi.org/10.1002/essoar.10505486.1>, 2020.
- 710 Ma, L., Hurtt, G., Tang, H., Lamb, R. L., Campbell, E., Dubayah, R. O., Guy, M., Huang, W., Lister, A. and Lu, J.:  
711 High-resolution forest carbon modeling for climate mitigation planning over the RGGI region, USA, Environmental  
712 Research Letters, <https://doi.org/10.1088/1748-9326/abe4f4>, 2021.
- 713 Markus, T., Neumann, T., Martino, A., Abdalati, W., Brunt, K., Csatho, B., Farrell, S., Fricker, H., Gardner, A.,  
714 Harding, D., Jasinski, M., Kwok, R., Magruder, L., Lubin, D., Luthcke, S., Morison, J., Nelson, R.,  
715 Neuenschwander, A., Palm, S., Popescu, S., Shum, C., Schutz, B. E., Smith, B., Yang, Y. and Zwally, J.: The Ice,  
716 Cloud, and land Elevation Satellite-2 (ICESat-2): Science requirements, concept, and implementation, Remote  
717 Sensing of Environment, 190, 260–273, <https://doi.org/10.1016/j.rse.2016.12.029>, 2017.
- 718 Massad, R.-S., Tuzet, A. and Bethenod, O.: The effect of temperature on C4-type leaf photosynthesis parameters,  
719 Plant, Cell & Environment, 30(9), 1191–1204, <https://doi.org/10.1111/j.1365-3040.2007.01691.x>, 2007.
- 720 Massoud, E. C., Xu, C., Fisher, R. A., Knox, R. G., Walker, A. P., Serbin, S. P., Christoffersen, B. O., Holm, J. A.,  
721 Kueppers, L. M., and Ricciuto, D. M.: Identification of key parameters controlling demographically structured  
722 vegetation dynamics in a land surface model: CLM4. 5 (FATES), Geoscientific Model Development, 12, 4133–  
723 4164, 2019.
- 724 Medvigy, D.: The State of the Regional Carbon Cycle: Results from a Constrained Coupled Ecosystem-atmosphere  
725 Model, Ph.D thesis, Harvard University, Cambridge, Massachusetts  
726 <https://books.google.com/books?id=ZJJwYGEAAAJ>, 2006.
- 727 Medvigy, D., Wofsy, S. C., Munger, J. W., Hollinger, D. Y. and Moorcroft, P. R.: Mechanistic scaling of ecosystem  
728 function and dynamics in space and time: Ecosystem Demography model version 2, Journal of Geophysical  
729 Research: Biogeosciences, 114(G1), <https://doi.org/10.1029/2008JG000812>, 2009.
- 730 Mercado, L. M., Bellouin, N., Sitch, S., Boucher, O., Huntingford, C., Wild, M. and Cox, P. M.: Impact of changes  
731 in diffuse radiation on the global land carbon sink, Nature, 458(7241), 1014–1017, 2009.
- 732 Monteith, J.: Evaporation and environment, Symposia of the Society for Experimental Biology, 19, 205–234, 1965.
- 733 Montzka, C., Herbst, M., Weihermüller, L., Verhoef, A. and Vereecken, H.: A global data set of soil hydraulic  
734 properties and sub-grid variability of soil water retention and hydraulic conductivity curves, Earth System Science  
735 Data, 9(2), 529–543, 2017.
- 736 Moorcroft, P. R., Hurtt, G. C. and Pacala, S. W.: A Method for Scaling Vegetation Dynamics: The Ecosystem  
737 Demography Model (ed), Ecological Monographs, 71(4), 557–586, [https://doi.org/10.1890/0012-9615\(2001\)071\[0557:AMFSVD\]2.0.CO;2](https://doi.org/10.1890/0012-9615(2001)071[0557:AMFSVD]2.0.CO;2), 2001.
- 739 Mu, Q., Zhao, M., and Running, S. W.: Improvements to a MODIS global terrestrial evapotranspiration algorithm,  
740 115, 1781–1800, 2011.
- 741  
742 Murray-Tortarolo, G., Anav, A., Friedlingstein, P., Sitch, S., Piao, S., Zhu, Z., Poulter, B., Zaehle, S., Ahlström, A.,  
743 Lomas, M., Levis, S., Viovy, N. and Zeng, N.: Evaluation of Land Surface Models in Reproducing Satellite-Derived  
744 LAI over the High-Latitude Northern Hemisphere. Part I: Uncoupled DGVMs, Remote Sensing, 5(10), 4819–4838,  
745 <https://doi.org/10.3390/rs5104819>, 2013.
- 746 Myneni, R., Knyazikhin, Y. and Park: MCD15A3H MODIS/Terra+Aqua Leaf Area Index/FPAR 4-day L4 Global  
747 500m SIN Grid V006, , <https://doi.org/10.5067/MODIS/MCD15A3H.006>, 2015.
- 748 Neilson, R. P.: A model for predicting continental-scale vegetation distribution and water balance, 5, 362–385,  
749 1995.
- 750 Neuenschwander, A. L., Popescu, S. C., Nelson, R. F., Harding, D., Pitts, K. L. and Robbins, J.: ATLAS/ICESat-2  
751 L3A Land and Vegetation Height, version 3, , <https://doi.org/10.5067/ATLAS/ATL08.003>, 2020.



- 752 Ott, L., Hurtt, G. C., Randerson, J. T., Chatterjee, A., Chen, Y., Chini, L. P., Davis, S. J., Hubacek, K., Lee, E., MA,  
753 L., Poulter, B., Rousseaux, C. S., Sun, L., Woodard, D. and Zeng, F.: Toward integrated seasonal predictions of land  
754 and ocean carbon flux: lessons from the 2015-16 El Nino, AGU Fall Meeting Abstracts, 51  
755 <http://adsabs.harvard.edu/abs/2018AGUFM.B51E1990O>, last access: 24 November 2020, 2018.
- 756 Pacala, S. W., Canham, C. D., Saponara, J., Silander Jr, J. A., Kobe, R. K. and Ribbens, E.: Forest models defined  
757 by field measurements: estimation, error analysis and dynamics, *Ecological monographs*, 66(1), 1–43, 1996.
- 758 Parton, W. J.: The CENTURY model, in: *Evaluation of soil organic matter models*, Springer, 283–291, 1996.
- 759 Peters, W., Jacobson, A. R., Sweeney, C., Andrews, A. E., Conway, T. J., Masarie, K., Miller, J. B., Bruhwiler, L.  
760 M. P., Pétron, G., Hirsch, A. I., Worthy, D. E. J., van der Werf, G. R., Randerson, J. T., Wennberg, P. O., Krol, M.  
761 C. and Tans, P. P.: An atmospheric perspective on North American carbon dioxide exchange: CarbonTracker, *Proc  
762 Natl Acad Sci USA*, 104(48), 18925, <https://doi.org/10.1073/pnas.0708986104>, 2007.
- 763 Peylin, P., Law, R., Gurney, K., Chevallier, F., Jacobson, A., Maki, T., Niwa, Y., Patra, P., Peters, W. and Rayner,  
764 P.: Global atmospheric carbon budget: results from an ensemble of atmospheric CO<sub>2</sub> inversions, *Biogeosciences*,  
765 10(10), 6699–6720, 2013.
- 766 Pielke Sr., R. A., Pitman, A., Niyogi, D., Mahmood, R., McAlpine, C., Hossain, F., Goldewijk, K. K., Nair, U.,  
767 Betts, R., Fall, S., Reichstein, M., Kabat, P. and de Noblet, N.: Land use/land cover changes and climate: modeling  
768 analysis and observational evidence, *WIREs Climate Change*, 2(6), 828–850, <https://doi.org/10.1002/wcc.144>, 2011.
- 769 Potter, C. S., Randerson, J. T., Field, C. B., Matson, P. A., Vitousek, P. M., Mooney, H. A., and Klooster, S. A.:  
770 Terrestrial ecosystem production: A process model based on global satellite and surface data, 7, 811–841,  
771 <https://doi.org/10.1029/93GB02725>, 1993.
- 772 Poulter, B., MacBean, N., Hartley, A., Khlystova, I., Arino, O., Betts, R., Bontemps, S., Boettcher, M., Brockmann,  
773 C., Defourny, P., Hagemann, S., Herold, M., Kirches, G., Lamarche, C., Lederer, D., Otlé, C., Peters, M. and  
774 Peylin, P.: Plant functional type classification for earth system models: results from the European Space Agency’s  
775 Land Cover Climate Change Initiative, *Geoscientific Model Development*, 8(7), 2315–2328,  
776 <https://doi.org/10.5194/gmd-8-2315-2015>, 2015.
- 777 Prentice, I. C., Cramer, W., Harrison, S. P., Leemans, R., Monserud, R. A., and Solomon, A. M.: Special paper: a  
778 global biome model based on plant physiology and dominance, soil properties and climate, 117–134, 1992.
- 779 Prentice, I. C. and Cowling, S. A.: Dynamic global vegetation models, *Encyclopedia of biodiversity*, 670–689,  
780 <https://doi.org/10.1016/B978-0-12-384719-5.00412-3>, 2013.
- 781 Prentice, I. C., Bondeau, A., Cramer, W., Harrison, S. P., Hickler, T., Lucht, W., Sitch, S., Smith, B. and Sykes, M.  
782 T.: Dynamic Global Vegetation Modeling: Quantifying Terrestrial Ecosystem Responses to Large-Scale  
783 Environmental Change, in *Terrestrial Ecosystems in a Changing World*, edited by J. G. Canadell, D. E. Pataki, and  
784 L. F. Pitelka, pp. 175–192, Springer, Berlin, Heidelberg, [https://doi.org/10.1007/978-3-540-32730-1\\_15](https://doi.org/10.1007/978-3-540-32730-1_15), , 2007.
- 785 Raich, J. W., Rastetter, E. B., Melillo, J. M., Kicklighter, D. W., Stuedler, P. A., Peterson, B. J., Grace, A. L.,  
786 Moore, B., and Vorosmarty, C. J.: Potential Net Primary Productivity in South America: Application of a Global  
787 Model, 1, 399–429, <https://doi.org/10.2307/1941899>, 1991.
- 788 Randerson, J. T., Hoffman, F. M., Thornton, P. E., Mahowald, N. M., Lindsay, K., LEE, Y.-H., Nevison, C. D.,  
789 Doney, S. C., Bonan, G., and Stöckli, R.: Systematic assessment of terrestrial biogeochemistry in coupled climate–  
790 carbon models, 15, 2462–2484, 2009.
- 791 Randerson, J., Van Der Werf, G., Giglio, L., Collatz, G. and Kasibhatla, P.: Global Fire Emissions Database,  
792 Version 4.1 (GFEDv4), ORNL DAAC, 2015.
- 793 Reich, P. B., Walters, M. B. and Ellsworth, D. S.: From tropics to tundra: Global convergence in plant functioning,  
794 *Proc Natl Acad Sci USA*, 94(25), 13730, <https://doi.org/10.1073/pnas.94.25.13730>, 1997.



- 795 Rödenbeck, C., Le Quéré, C., Heimann, M. and Keeling, R. F.: Interannual variability in oceanic biogeochemical  
796 processes inferred by inversion of atmospheric O<sub>2</sub>/N<sub>2</sub> and CO<sub>2</sub> data, *null*, 60(5), 685–705,  
797 <https://doi.org/10.1111/j.1600-0889.2008.00375.x>, 2008.
- 798 Santoro, M., Cartus, O., Mermoz, S., Bouvet, A., Le Toan, T., Carvalhais, N., Rozendaal, D., Herold, M., Avitabile,  
799 V., Quegan, S., Carreiras, J., Rauste, Y., Balzter, H., Schmullius, C. and Seifert, F. M.: GlobBiomass - global  
800 datasets of forest biomass, , 174 data points, <https://doi.org/10.1594/PANGAEA.894711>, 2018.
- 801 Sato, H., Itoh, A., and Kohyama, T.: SEIB–DGVM: A new Dynamic Global Vegetation Model using a spatially  
802 explicit individual-based approach, 200, 279–307, 2007.
- 803 Sellers, P. J., Mintz, Y., Sud, Y. C., and Dalcher, A.: A Simple Biosphere Model (SIB) for Use within General  
804 Circulation Models, 43, 505–531, [https://doi.org/10.1175/1520-0469\(1986\)043<0505:ASBMFU>2.0.CO;2](https://doi.org/10.1175/1520-0469(1986)043<0505:ASBMFU>2.0.CO;2), 1986.  
805
- 806 Shugart, H. H. and West, D.: Development of an Appalachian deciduous forest succession model and its application  
807 to assessment of the impact of the chestnut blight., 1977.
- 808 Shugart, H. H., Wang, B., Fischer, R., Ma, J., Fang, J., Yan, X., Huth, A. and Armstrong, A. H.: Gap models and  
809 their individual-based relatives in the assessment of the consequences of global change, *Environmental Research*  
810 *Letters*, 13(3), 033001, <https://doi.org/10.1088/1748-9326/aaaacc>, 2018.
- 811 Sitch, S., Huntingford, C., Gedney, N., Levy, P. E., Lomas, M., Piao, S. L., Betts, R., Ciais, P., Cox, P.,  
812 Friedlingstein, P., Jones, C. D., Prentice, I. C. and Woodward, F. I.: Evaluation of the terrestrial carbon cycle, future  
813 plant geography and climate-carbon cycle feedbacks using five Dynamic Global Vegetation Models (DGVMs),  
814 *Global Change Biology*, 14(9), 2015–2039, <https://doi.org/10.1111/j.1365-2486.2008.01626.x>, 2008.
- 815 Smith, B., Prentice, I. C., and Sykes, M. T.: Representation of vegetation dynamics in the modelling of terrestrial  
816 ecosystems: comparing two contrasting approaches within European climate space, 621–637, 2001.  
817
- 818 Smith, B., Wårlind, D., Arneth, A., Hickler, T., Leadley, P., Siltberg, J., and Zaehle, S.: Implications of  
819 incorporating N cycling and N limitations on primary production in an individual-based dynamic vegetation model,  
820 11, 2027–2054, 2014.
- 821 Spawn, S. A., Sullivan, C. C., Lark, T. J. and Gibbs, H. K.: Harmonized global maps of above and belowground  
822 biomass carbon density in the year 2010, *Scientific Data*, 7(1), 112, <https://doi.org/10.1038/s41597-020-0444-4>,  
823 2020.
- 824 Todd-Brown, K. E. O., Randerson, J. T., Post, W. M., Hoffman, F. M., Tarnocai, C., Schuur, E. a. G. and Allison, S.  
825 D.: Causes of variation in soil carbon simulations from CMIP5 Earth system models and comparison with  
826 observations, *Biogeosciences*, 10(3), 1717–1736, <https://doi.org/10.5194/bg-10-1717-2013>, 2013.
- 827 Verger, A., Baret, F. and Weiss, M.: Near Real-Time Vegetation Monitoring at Global Scale, *IEEE Journal of*  
828 *Selected Topics in Applied Earth Observations and Remote Sensing*, 7(8), 3473–3481,  
829 <https://doi.org/10.1109/JSTARS.2014.2328632>, 2014.
- 830 Walther, G.-R., Post, E., Convey, P., Menzel, A., Parmesan, C., Beebee, T. J. C., Fromentin, J.-M., Hoegh-  
831 Guldberg, O. and Bairlein, F.: Ecological responses to recent climate change, *Nature*, 416(6879), 389–395,  
832 <https://doi.org/10.1038/416389a>, 2002.
- 833 Weng, E. S., Malyshev, S., Lichstein, J. W., Farrior, C. E., Dybzinski, R., Zhang, T., Shevliakova, E., and Pacala, S.  
834 W.: Scaling from individual trees to forests in an Earth system modeling framework using a mathematically  
835 tractable model of height-structured competition, 12, 2655–2694, 2015.
- 836 Wieder, W. R., Boehnert, J., Bonan, G. B. and Langseth, M.: RegridDED Harmonized World Soil Database v1.2,  
837 ORNL DAAC, <https://doi.org/10.3334/ORNLDAAC/1247>, 2014.
- 838 Yang, X., Tang, J., Mustard, J. F., Lee, J.-E., Rossini, M., Joiner, J., Munger, J. W., Kornfeld, A. and Richardson, A.  
839 D.: Solar-induced chlorophyll fluorescence that correlates with canopy photosynthesis on diurnal and seasonal



840 scales in a temperate deciduous forest, *Geophysical Research Letters*, 42(8), 2977–2987,  
841 <https://doi.org/10.1002/2015GL063201>, 2015.

842 Zhang, Y., Joiner, J., Alemohammad, S. H., Zhou, S. and Gentine, P.: A global spatially contiguous solar-induced  
843 fluorescence (CSIF) dataset using neural networks, *Biogeosciences*, 15(19), 5779–5800, 2018.

844  
845



846 **Figures and Tables**

847

848

849

Table 1. Summary of benchmarking datasets used for evaluation of ED model.

Variable	Source	Description	Reference
Vegetation distribution			
PFT	ESA CCI	Global gridded, 300-m, 2015	ESA (2017)
Carbon stocks			
AGB	Santoro et al. (2018)	Global gridded, 100-m, 2010	Santoro et al. (2018)
	Spawn et al. (2020)	Global gridded, 300-m, 2010	Spawn et al. (2020)
Soil carbon	HWSD	Gridded, 0.05 degree, 2000	Wieder et al. (2014)
Carbon and water fluxes			
GPP	FLUXCOM (RS+METEO, CRUIA and ERA5)	Global gridded, 0.0833-degree, 1979-2017 monthly	Jung et al. (2020)
	FluxSat	Global gridded, 0.05-degree, 2001-2018 monthly	Joiner et al. (2018)
NBP	CAMS (v17r1)	Global gridded, 1.875x3.75-degree, 1979-2017 monthly	Chevallier et al. (2005)
	Jena CarbonScope (s81oc_v2020)	Global gridded, 2.5x2.0 degree, 1981-2016 daily	Rödenbeck et al. (2008)
	CarbonTracker Europe (CTE)	Global gridded, 1x1 degree, 2000-2016 monthly	van der Laan-Luijkx et al. (2017)
	GCB2020 DGVMs	Global total, 1959-2019 yearly	Friedlingstein et al. (2020)
	GCB2020 Residual sink	Global total, 1959-2019 yearly	Friedlingstein et al. (2020)
ET	FLUXCOM (RS+METEO, CRUNCEP and GSWP3)	Global gridded, 0.0833-degree, 1981-2014 monthly	Jung et al. (2020)
Vegetation structure			
Tree height	GEDI L2A (v001)	51°N ~ 51°S, 20-m footprint, 2019-2020	Dubayah et al. (2020c)
	ICESat-2 ATL08 (v003)	51°N ~ 51°S, 100-m footprint, 2018-2020	Neuenschwander et al. (2020)
LAI	MODIS MCD15A3H (v006)	Global gridded, 500-m, 2003-2016 4-day	Myneni et al. (2015)
	GEOV2	Global gridded, 1/3-km, 1999-2016 10-day	Verger et al. (2014)
Vertical LAI	GEDI L2B (v001)	51°N ~ 51°S, 20-m footprint, 2019-2020	Dubayah et al. (2020b)

850

851

852

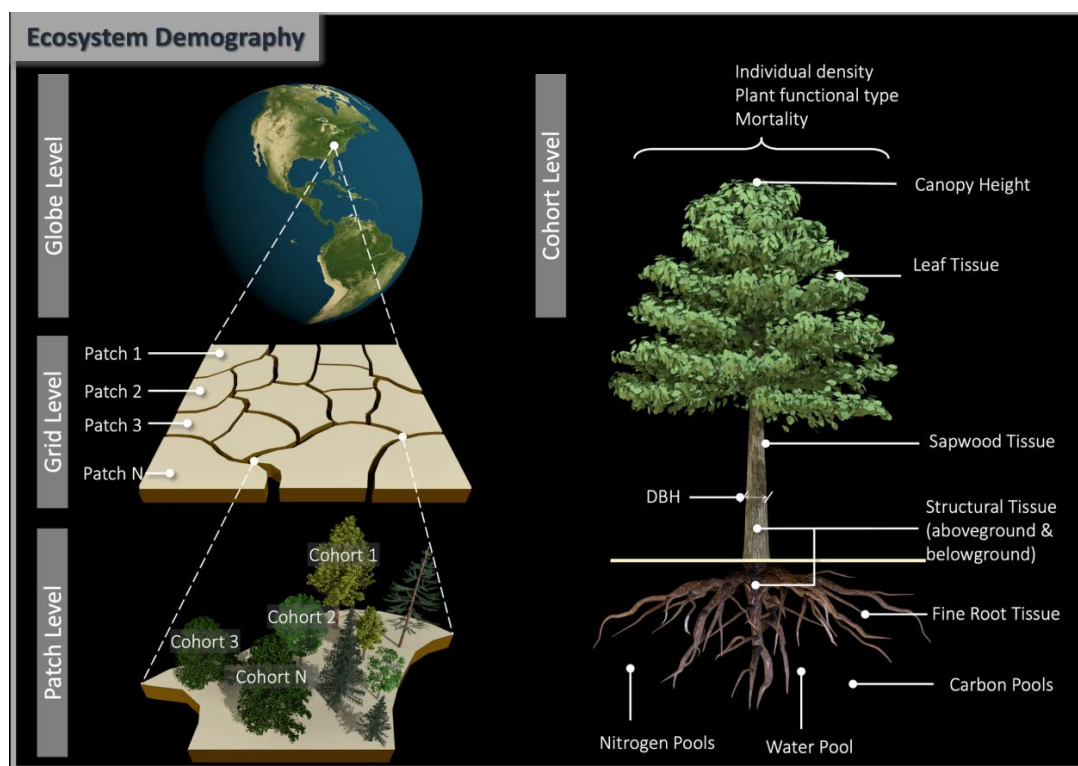


Figure 1. Diagram of vegetation representation scheme in ED model. Globe consists of land grids with fixed spatial resolution. A grid consists of patches with different ages from last disturbance and land use types, and patch areas dynamically change over time as a result of disturbance and land use changes. A patch consists of consists with different plant functional types and sizes. Plants in a cohort are depicted by properties including individual density, canopy height, diameter at breast (DBH), and biomass in leaf, sapwood, structural tissue and fine roots, and all these properties are simulated as a result of interaction with environment and other cohorts. Note that not all properties are shown here.

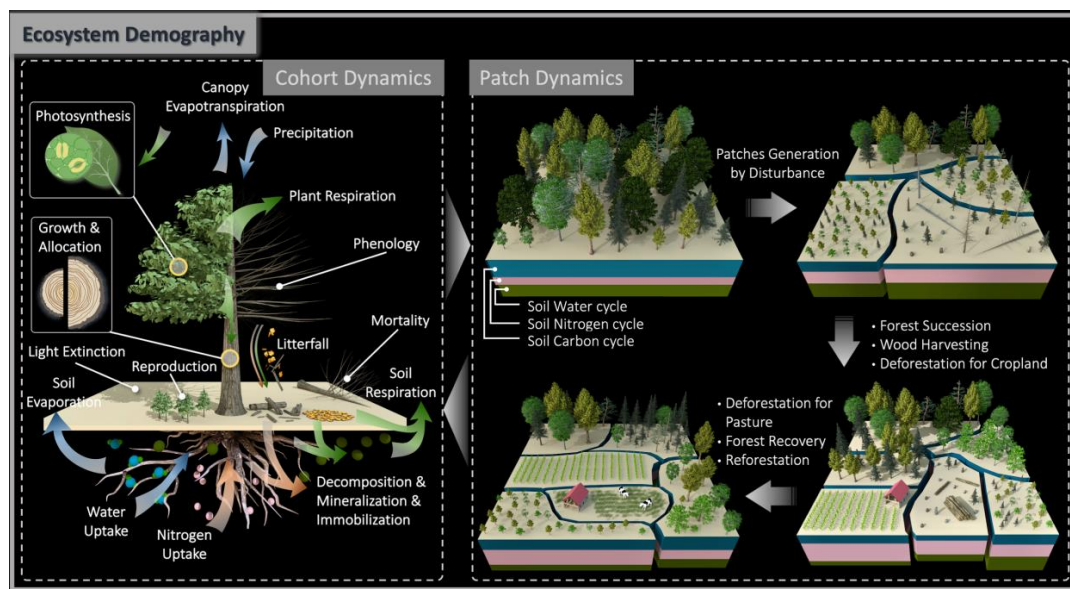


Figure 2. Schematic diagram of processes represented in ED model. Dynamics at cohort level consists of carbon-related flow (green arrow), water-related flow (blue arrow) and nitrogen-related (orange arrow). Carbon dynamics include carbon assimilation by photosynthesis, carbon allocation for plant growth in height/DBH, reproduction and respiration, carbon translocation between plants and soil through tissue turnover as litterfall and dead plants due to mortality, and carbon decomposition and respiration in soil carbon pools. Water dynamics include water inputs from precipitation and infiltration into soil, uptake by vegetation and evaporation and transpiration of soil and canopy. Nitrogen dynamics includes nitrogen uptake from soil pools, translocation from vegetation to soil through litterfall and dead plants, and mineralization and immobilization in soil. Note that not all processes that ED characterize are depicted here. Dynamics at patch level consist of consequences from a variety of disturbance events both natural and anthropogenic. Patch dynamics include disturbance-driven patch heterogenization in age and areas, forest succession, wood harvesting, deforestation for cropland and pasture expansion, and forest recovery and reforestation from abandoned cropland, harvested forest and pasture.

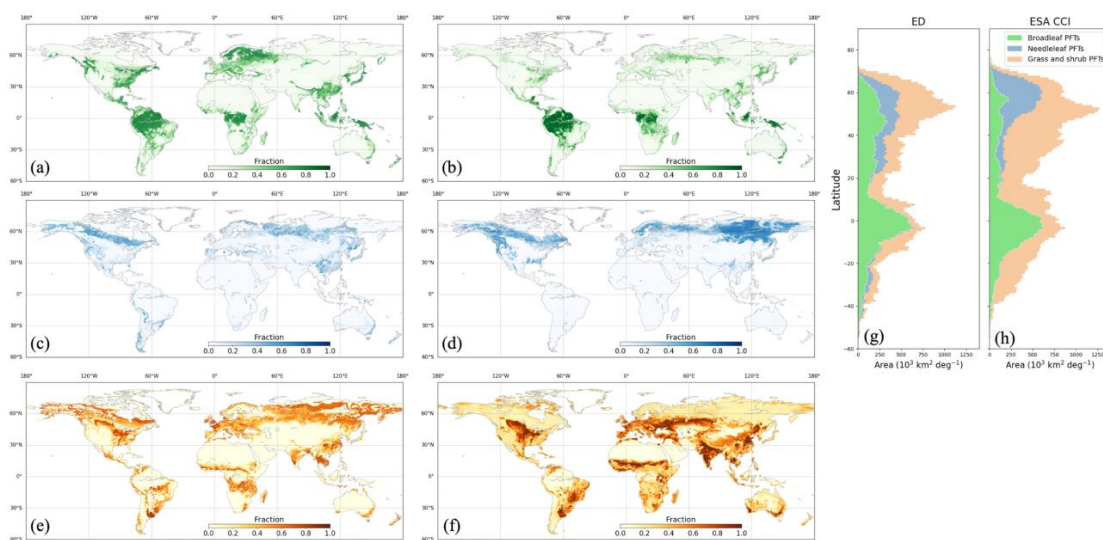


Figure 3. Spatial distribution of broadleaf PFTs, needleleaf and PFTs and grass and shrub PFTs in 2015 from ED (a), (c) and (e), and from ESA CCI (b), (d) and (f). Corresponding latitudinal total area is compared in (g) and (h).

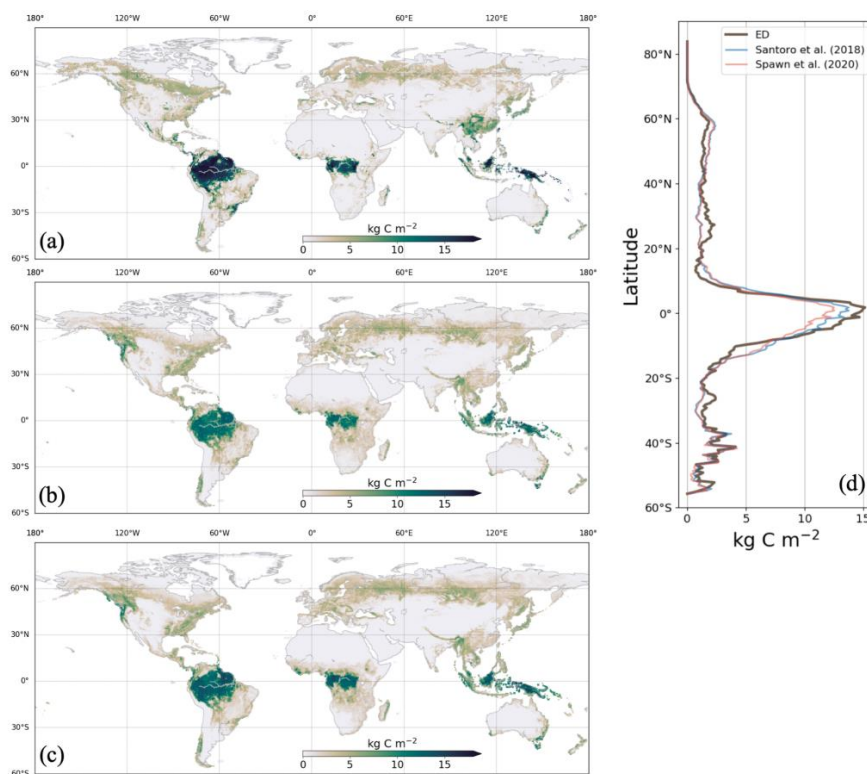


Figure 4. AGB in 2010 from ED (a), Spawn et al., (2020) (b), and Santoro et al., (2018) (c), with latitudinal average AGB compared in (d).

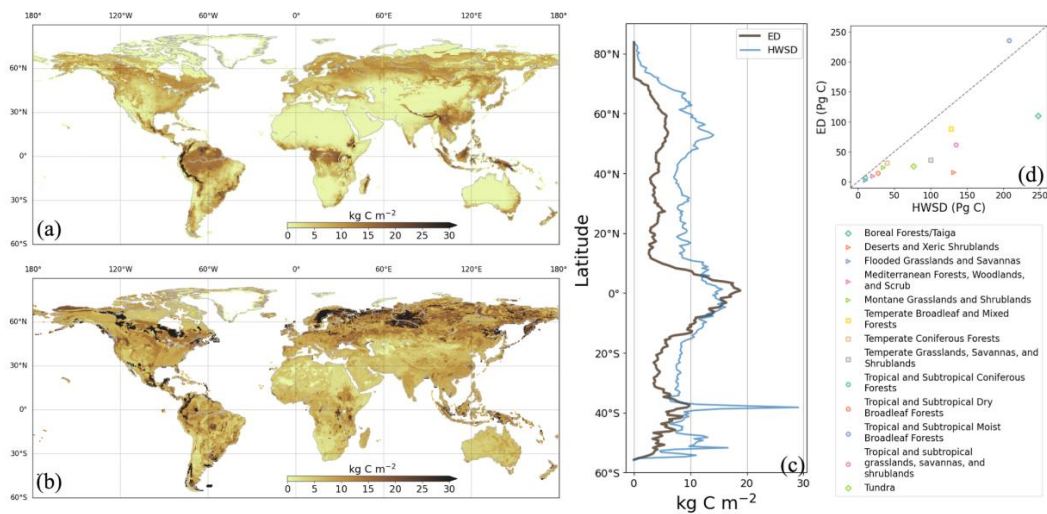


Figure 5. Soil carbon density in 2000 from ED (a) and HWSO (b). Latitudinal average density and total stocks per biome are compared in (c) and (d), respectively.

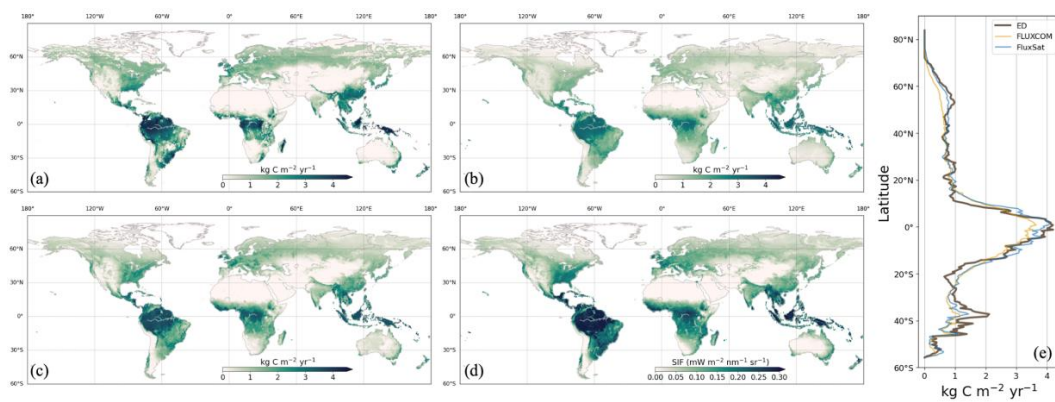


Figure 6. Average annual GPP between 2001 and 2016 from ED (a), FLUXCOM (b), FluxSat (c) and CSIF (d). Comparison of latitudinal average GPP is shown in (e).

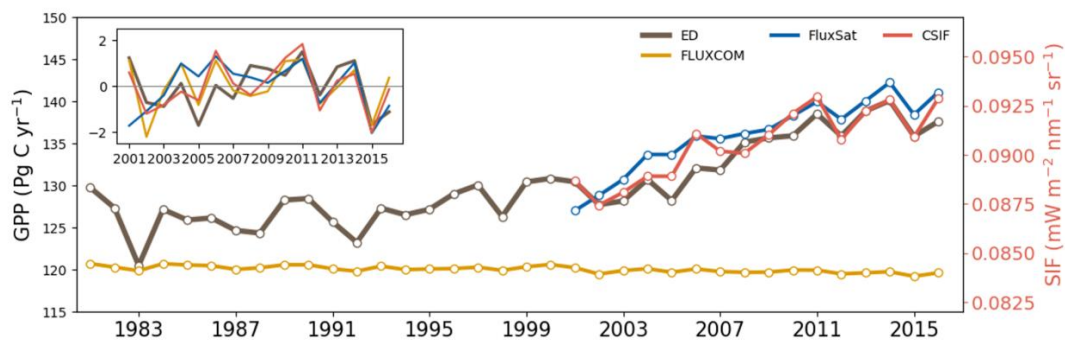


Figure 7. Time-series of global annual total GPP from ED, FLUXCOM, and FluxSat, and global annual average CSIF. Their interannual anomaly is shown in the inset.

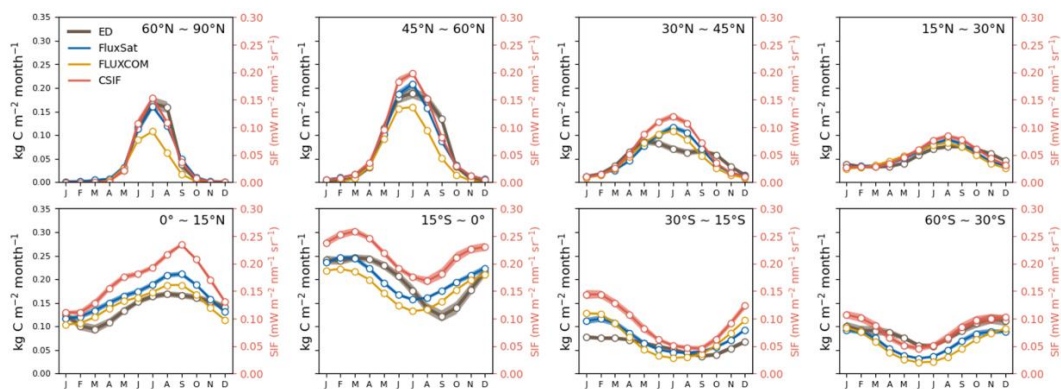


Figure 8. Average seasonal cycle (2001-2016) of GPP from ED, FLUXCOM, FluxSat, and CSIF by latitudinal band.

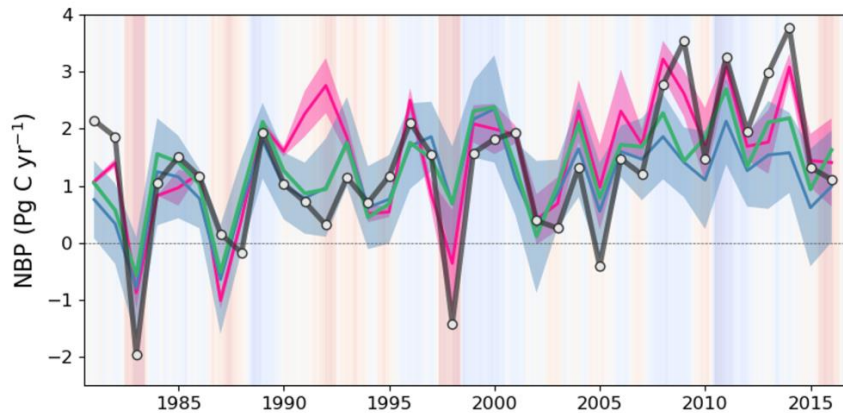


Figure 9. Global annual NBP between 1981 and 2016 from ED (black line), DGVMs from the GCB2020 (ensemble average shown in blue line with  $\pm 1\sigma$  spread shown in blue shading), the ensemble of atmospheric inversions (ensemble average shown in pink line with  $\pm 1\sigma$  spread shown in pink shading), and the terrestrial residual sink of the GCB2020 (green line). Positive values indicate net carbon uptake from land. Background shading represents the bi-monthly Multivariate El Niño/Southern Oscillation (ENSO) index, where red indicates El Niño and blue indicates La Niña.

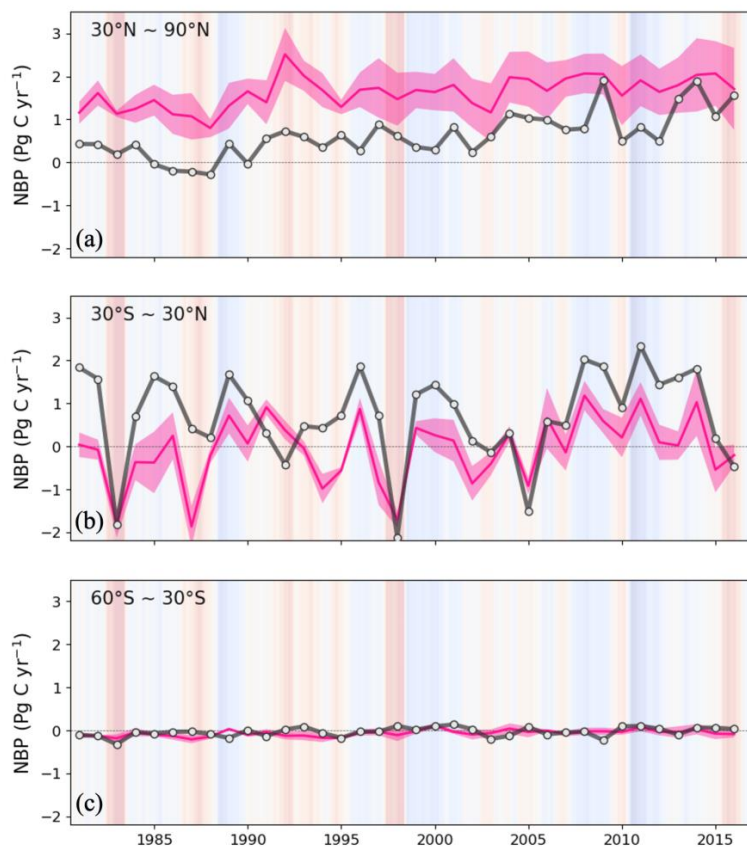


Figure 10. Annual NBP between 1981 and 2016 from ED and ensemble of atmospheric inversions for the Northern Hemisphere ( $>30^{\circ}\text{N}$ ) (a), tropics ( $30^{\circ}\text{N} - 30^{\circ}\text{S}$ ) (b) and the Southern Hemisphere ( $<30^{\circ}\text{S}$ ) (c). Black line is ED, and the pink line and pink shading are the inversion ensemble average and  $\pm 1\sigma$  spread of atmospheric inversions, respectively.

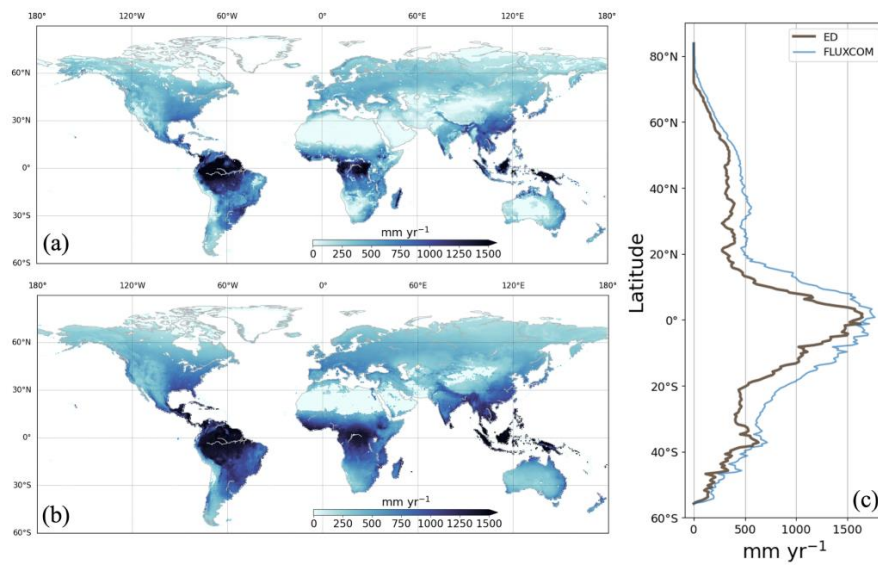


Figure 11. Average annual ET between 1981 and 2016 from ED (a) and FLUXCOM (b) with corresponding latitudinal average comparison (c).

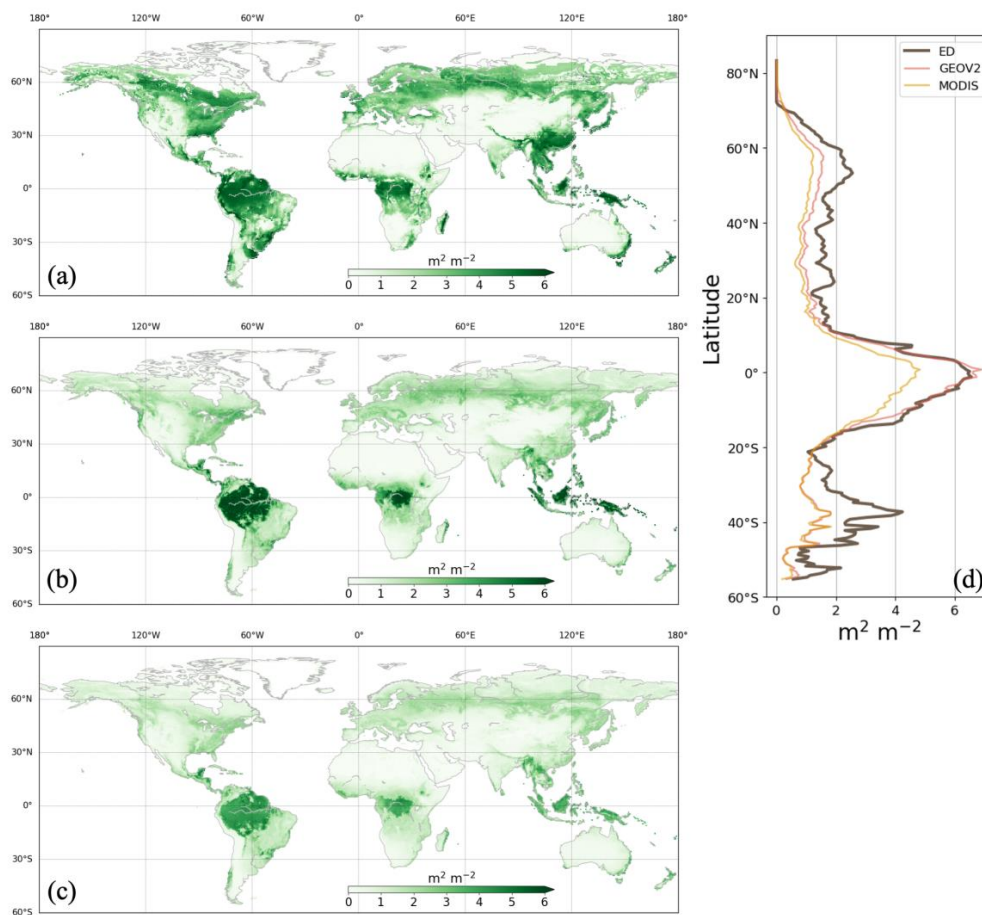


Figure 12. Average LAI during the growing season between 2003 and 2016 from ED (a), GEOV2 (b), and MODIS (c). Corresponding latitudinal averages are compared in (e). Growing season is defined as the months during which the average air temperature of MERRA2 is above 0°C.

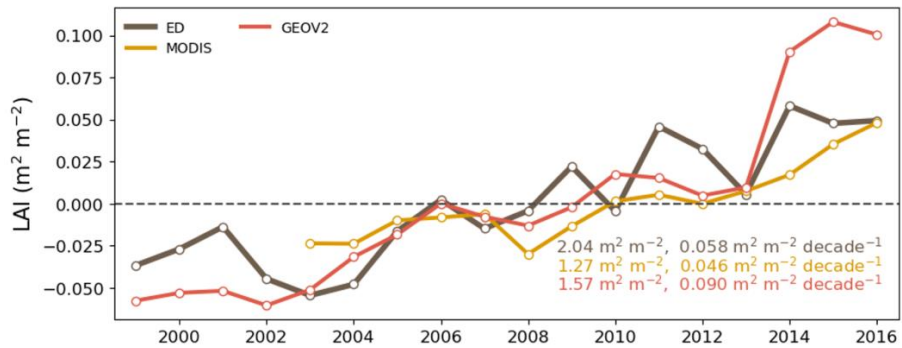


Figure 13. Interannual global average growing season LAI from ED, MODIS and GEOV2. The anomaly is calculated by subtracting annual LAI by multi-year average.

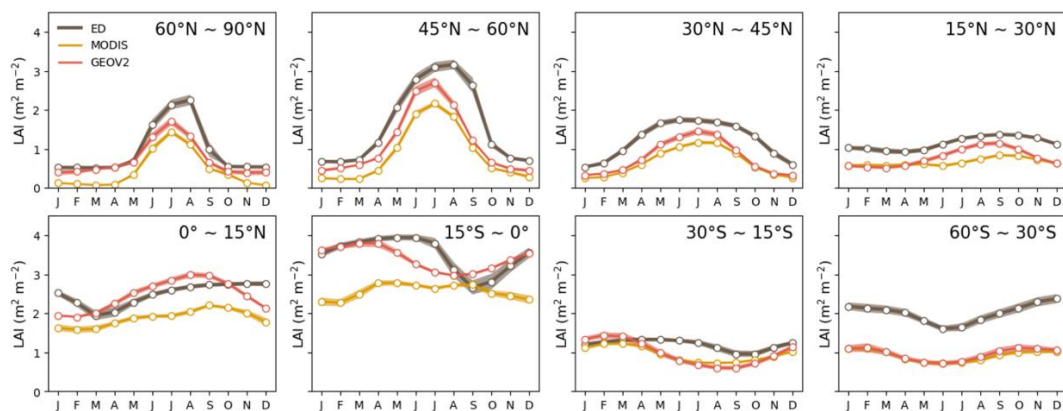


Figure 14. Seasonal LAI by latitudinal band from ED, MODIS and GEOV2.

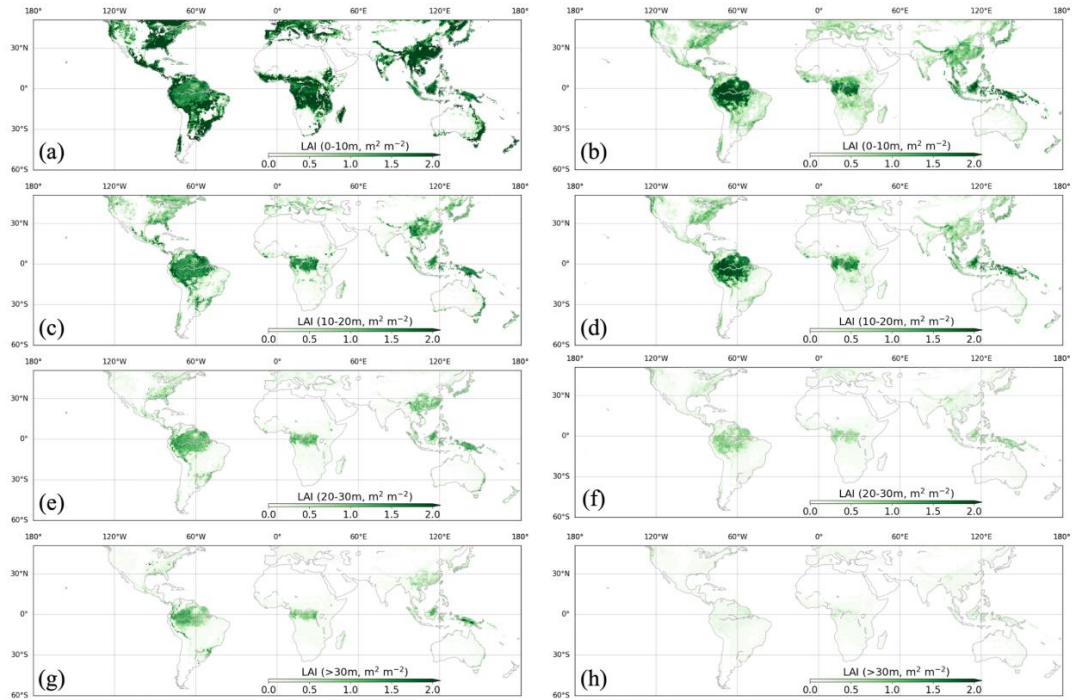


Figure 15. Vertical LAI from ED (left column) and GEDI L2B (right column) at height (0-10m) in (a) and (b), 10-20m in (c) and (d), 20-30m in (e) and (f), and above 30m in (g) and (h), respectively.

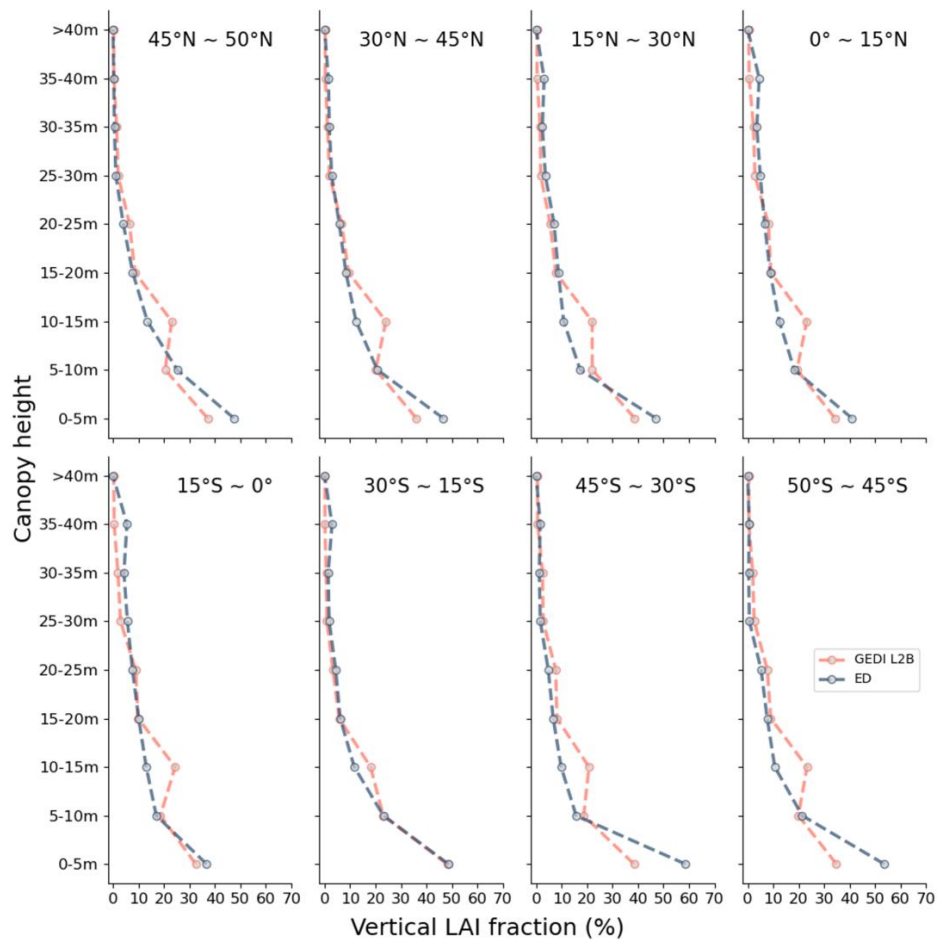


Figure 16. Relative fraction of vertical LAI by latitudinal band between ED and GEDI L2B.

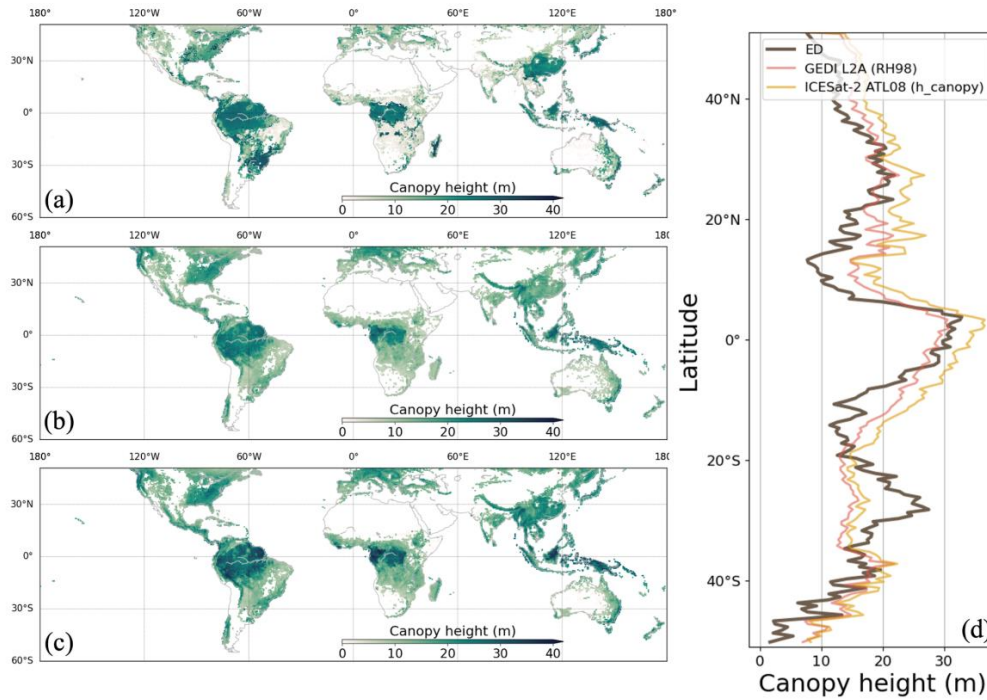


Figure 17. Canopy height from ED (a), GEDI L2A (b), and ICESat-2 ATL08 (c). Latitudinal averages are compared in (d). ESA CCI data grids with tree fractions below 5% are masked.